








Scaling of Turbulent Viscosity and Resistivity: Extracting a Scale-dependent Turbulent Magnetic Prandtl Number

Xin Bian¹ , Jessica K. Shang¹ , Eric G. Blackman² , Gilbert W. Collins^{1,2,3} , and Hussein Aluie^{1,3} 

¹Department of Mechanical Engineering, University of Rochester, NY 14627, USA; hussein@rochester.edu

²Department of Physics and Astronomy, University of Rochester, NY 14627, USA

³Laboratory for Laser Energetics, University of Rochester, NY 14623, USA

Received 2021 March 5; revised 2021 June 25; accepted 2021 June 29; published 2021 August 9

Abstract

Turbulent viscosity ν_t and resistivity η_t are perhaps the simplest models for turbulent transport of angular momentum and magnetic fields, respectively. The associated turbulent magnetic Prandtl number $\text{Pr}_t \equiv \nu_t/\eta_t$ has been well recognized to determine the final magnetic configuration of accretion disks. Here, we present an approach to determining these “effective transport” coefficients acting at different length scales using coarse-graining and recent results on decoupled kinetic and magnetic energy cascades. By analyzing the kinetic and magnetic energy cascades from a suite of high-resolution simulations, we show that our definitions of ν_t , η_t , and Pr_t have power-law scalings in the “decoupled range.” We observe that $\text{Pr}_t \approx 1-2$ at the smallest inertial-inductive scales, increasing to ≈ 5 at the largest scales. However, based on physical considerations, our analysis suggests that Pr_t has to become scale independent and of order unity in the decoupled range at sufficiently high Reynolds numbers (or grid resolution) and that the power-law scaling exponents of velocity and magnetic spectra become equal. In addition to implications for astrophysical systems, the scale-dependent turbulent transport coefficients offer a guide for large-eddy simulation modeling.

Unified Astronomy Thesaurus concepts: [Magnetohydrodynamics \(1964\)](#); [Magnetic fields \(994\)](#); [Magnetohydrodynamical simulations \(1966\)](#)

1. Introduction

Magnetohydrodynamic (MHD) turbulence is central to our understanding of many astrophysical systems, including the solar wind, interstellar medium (ISM), and accretion disks.

Most of these systems are characterized by very large Reynolds numbers (Re). For example, $\text{Re} \sim 10^5-10^7$ in the cool ISM (Elmegreen & Scalo 2004), $\text{Re} \sim 4 \times 10^6$ in the solar wind (Verma 1996), and $\text{Re} \sim 10^{14}$ in Type Ia supernovae (Kuhlen et al. 2006). High- Re turbulent flows involve a wide range of dynamical scales, called the “inertial-inductive” range, over which the evolutions of the flow and magnetic field are immune from the direct effects of external forcing and microphysical dissipation. Similar to hydrodynamic turbulence, it is widely expected that MHD turbulence over the inertial-inductive range has universal statistics with power-law spectra, although details of such a scaling remain a subject of debate (Goldreich & Sridhar 1995; Biskamp 2003; Verma 2004, 2019; Zhou et al. 2004; Boldyrev 2005; Schekochihin 2020). While the large scales in a high- Re MHD flow are immune from the direct effects of microphysical transport (Aluie 2017; Zhao & Aluie 2018), they are indirectly influenced by the microphysics due to the “catalytic” role of turbulence via the cascade process, which acts as a bridge between the large and microphysical scales. For example, it is widely believed that turbulence plays an important role in the outward transport of angular momentum in accretion disks for inward mass accretion (Balbus & Hawley 1998).

The simplest conceptual framework to think of turbulence is as an effective (or turbulent) viscosity ν_t , which leads to the “turbulent diffusion” of angular momentum at scales far larger than viscous scales, and has long shaped our thinking of accretion disk dynamics (Shakura & Sunyaev 1973). Similarly, magnetic fields,

which are essential for launching and collimating jets (Blandford & Znajek 1977; Blandford & Payne 1982; Jafari & Vishniac 2018), can be transported outward by an effective (or turbulent) resistivity η_t . In this way, the magnetic field configuration in accretion disks may be influenced by a balance between the inward advection by accretion and the outward diffusion by turbulent resistivity (Lubow et al. 1994; Fromang & Stone 2009; Guan & Gammie 2009; Lovelace et al. 2009; Cao 2011). This balance between the competing effects of ν_t and η_t is captured by the turbulent magnetic Prandtl number $\text{Pr}_t \equiv \nu_t/\eta_t$. Whether global-scale structures or turbulent stress dominates the overall angular momentum transport is still an open question and important for determining the budget of thermal versus nonthermal emission (Blackman & Nauman 2015).

For turbulent astrophysical flows, current computing resources are unable to solve all relevant scales. Large-eddy simulations (LESs) rely on subgrid-scale modeling to represent the small-scale effects on resolved scales (Meneveau & Katz 2000; Miesch et al. 2015). Müller & Carati (2002), Chernyshov et al. (2007), and Grete et al. (2015) studied different subgrid-scale (SGS) models. Renormalization group (RG) analysis was used to develop scale-dependent turbulent coefficients (Zhou 2010). However, the studies on MHD scale-dependent turbulent transport coefficients are few compared to hydrodynamic turbulence.

We remind readers that the turbulent magnetic Prandtl number is different from the microscopic magnetic Prandtl number $\text{Pr}_m \equiv \nu/\eta$, where ν is the microscopic viscosity, and η is the microscopic resistivity. Pr_m is large in the ISM while being small in stellar interiors and liquid metals (Davidson et al. 2012). Many studies have focused on the effect of Pr_m (e.g., Lesur & Longaretti 2007; Fromang & Stone 2009; Brandenburg 2014; Brandenburg & Rempel 2019). The extent

to which existing simulations accurately capture the physics of realistic extreme regimes of low and high Pr_m is uncertain.

In this paper we focus on Pr_r , not Pr_m . Turbulent transport coefficients have been studied both analytically and numerically. Estimates using mixing length theory $\nu_t \approx \eta_t \approx U\ell/3$ (characteristic velocity U and characteristic scale ℓ ; Yousef et al. 2003; Käpylä et al. 2020) are consistent to order of magnitude with η_t calculated with the test-field method (Käpylä et al. 2009) and shearing box simulations (Snellman et al. 2009). The quasilinear approximation (Kitchatinov et al. 1994; Yousef et al. 2003) and RG analysis (Forster et al. 1977; Fournier et al. 1982; Verma 2001a, 2001b) suggested that $0.4 < \text{Pr}_r < 0.8$. Zhou et al. (2002) developed eddy and backscatter viscosity and resistivity using eddy-damped quasilinear Markovian statistical closure model (EDQNM).

Numerical studies have traditionally identified “turbulence” as fluctuations from a (temporal or ensemble) mean flow and have typically yielded $\text{Pr}_r \approx 1$. Yousef et al. (2003) measured Pr_r from the decaying large-scale fields in forced turbulence simulations. The results showed that Pr_r is near unity and insensitive to Pr_m . These simulations were conducted with a fixed small magnetic Reynolds number. Several groups studied the turbulent transport coefficients using shearing box simulations (Fromang & Stone 2009; Guan & Gammie 2009; Lesur & Longaretti 2009). Guan & Gammie (2009) inferred η_t from the evolution of an imposed magnetic field perturbation in an already turbulent flow. Lesur & Longaretti (2009) imposed an external magnetic field and defined η_t using the electromotive force induced by the field. Fromang & Stone (2009) calculated η_t from the spatially varying magnetic fields induced by an electromotive term added in the induction equation. ν_t was defined using Reynolds and Maxwell stress tensors in these studies. Despite different definitions, numerical schemes, and magnetic field configurations among these studies, they all find $\text{Pr}_r \approx 1$. Käpylä et al. (2020) computed ν_t using both Reynolds stress and the decay rate of a large-scale field, and η_t using the test-field method, where a set of test fields are used to calculate the components of turbulent diffusivity tensors (Schinnerer et al. 2005, 2007). The results suggested that Pr_r increases with increasing Reynolds number and saturates at large Reynolds number with $0.8 \leq \text{Pr}_r \leq 0.95$.

Other than the RG and EDQNM analyses, the aforementioned studies did not analyze ν_t and η_t as a function of length scales, which is not possible from a Reynolds (mean versus fluctuation) decomposition (e.g., Fromang & Stone 2009; Guan & Gammie 2009; Lesur & Longaretti 2009; Käpylä et al. 2020). Determining the scale dependence of transport coefficients can improve the fidelity with which we characterize astrophysical turbulence in cohort with its practical application to subgrid-scale modeling. For example, if $\text{Pr}_r \propto \ell^\alpha$ with $\alpha > 0$, Pr_r grows at larger scales, indicating that the large-scale component of a flow, which is still part of the “fluctuations,” feels a stronger ν_t relative to η_t .

Our study aims to define and measure ν_t , η_t , and Pr_r at different scales using the coarse-graining approach (Eyink 2005; Aluie 2017) and the eddy-viscosity hypothesis (Boussinesq 1877). Our analytical and numerical results show power-law scaling of the turbulent transport coefficients in the “decoupled range” over which the kinetic and magnetic cascades statistically decouple and become conservative (Bian & Aluie 2019).

2. Methodology

2.1. Coarse-grained Energy Equations

We analyze the incompressible MHD equations with a constant density ρ :

$$\partial_t \mathbf{u} + (\mathbf{u} \cdot \nabla) \mathbf{u} = -\nabla p + \mathbf{J} \times \mathbf{B} + \nu \nabla^2 \mathbf{u} + \mathbf{f}, \quad (1)$$

$$\partial_t \mathbf{B} = \nabla \times (\mathbf{u} \times \mathbf{B}) + \eta \nabla^2 \mathbf{B}, \quad (2)$$

$$\nabla \cdot \mathbf{u} = \nabla \cdot \mathbf{B} = 0, \quad (3)$$

where \mathbf{u} is the velocity and \mathbf{B} is the magnetic field normalized by $\sqrt{4\pi\rho}$ to have Alfvén (velocity) units. p is pressure, $\mathbf{J} = \nabla \times \mathbf{B}$ is (normalized) current density, \mathbf{f} is external forcing, and ν and η are microscopic viscosity and resistivity, respectively.

We use the coarse-graining method to analyze the flow and define the turbulent magnetic Prandtl number. A coarse-grained field in n dimensions $\bar{f}_\ell(\mathbf{x}) = \int d^n \mathbf{r} G_\ell(\mathbf{x} - \mathbf{r}) f(\mathbf{r})$ contains modes at length scales greater than ℓ , where $G_\ell(\mathbf{r}) \equiv \ell^{-n} G(\mathbf{r}/\ell)$ is a normalized kernel with its main weight in a ball of diameter ℓ . The coarse-grained MHD equations for \bar{u}_ℓ , \bar{B}_ℓ , and the quadratic MHD invariants were shown by Aluie (2017). Hereafter, we drop subscript ℓ when possible.

The coarse-grained kinetic energy (KE) and magnetic energy (ME) density balance (at scales $> \ell$) are

$$\begin{aligned} \partial_t \left(\frac{|\bar{\mathbf{u}}|^2}{2} \right) + \nabla \cdot [\dots] \\ = -\bar{\Pi}_\ell^u - \bar{S}_{ij} \bar{B}_i \bar{B}_j - 2\nu |\bar{\mathbf{S}}|^2 + \bar{\mathbf{f}} \cdot \bar{\mathbf{u}}, \end{aligned} \quad (4)$$

$$\begin{aligned} \partial_t \left(\frac{|\bar{\mathbf{B}}|^2}{2} \right) + \nabla \cdot [\dots] \\ = -\bar{\Pi}_\ell^b + \bar{S}_{ij} \bar{B}_i \bar{B}_j - \eta |\bar{\mathbf{J}}|^2, \end{aligned} \quad (5)$$

where $\nabla \cdot [\dots]$ denotes spatial transport terms, $\mathbf{S} = (\nabla \mathbf{u} + \nabla \mathbf{u}^T)/2$ is the strain-rate tensor, and $\bar{\mathbf{f}} \cdot \bar{\mathbf{u}}$ is the energy injection rate at forcing scale $\ell_f = 2\pi/k_f$ (k_f are the modes of the forcing \mathbf{f}). Microscopic dissipation terms $\nu |\bar{\mathbf{S}}|^2$ and $\eta |\bar{\mathbf{J}}|^2$ are mathematically guaranteed (Aluie 2017; Eyink 2018) and numerically demonstrated (Zhao & Aluie 2018; Bian & Aluie 2019) to be negligible at scales $\ell \gg (\ell_\nu, \ell_\eta)$, where ℓ_ν and ℓ_η are the viscous and resistive length scales, respectively.

The KE cascade term $\bar{\Pi}_\ell^u \equiv -\bar{S}_\ell: \bar{\tau}_\ell$ in Equation (4) quantifies the KE transfer across scale ℓ , where $\bar{\tau}_{ij} \equiv \tau_\ell(u_i, u_j) - \tau_\ell(B_i, B_j)$ is the sum of subscale Reynolds and Maxwell stresses generated by scales $< \ell$ acting on the large-scale strain \bar{S}_{ij} , resulting in “turbulent viscous dissipation” to scales $< \ell$. Subscale stress is defined as $\tau_\ell(f, g) = \overline{(fg)_\ell} - \bar{f}_\ell \bar{g}_\ell$ for any two fields f and g . Similarly, the ME cascade term $\bar{\Pi}_\ell^b \equiv -\bar{\mathbf{J}}_\ell: \bar{\boldsymbol{\varepsilon}}_\ell$ in Equation (5) quantifies the ME transfer across scale ℓ , where the subscale electromotive force (EMF) $\bar{\boldsymbol{\varepsilon}}_\ell \equiv \mathbf{u} \times \mathbf{B} - \bar{\mathbf{u}} \times \bar{\mathbf{B}}$ is (minus) the electric field generated by scales $< \ell$ acting on the large-scale current $\bar{\mathbf{J}} = \nabla \times \bar{\mathbf{B}}$, resulting in “turbulent ohmic dissipation” to scales $< \ell$. Both $\bar{\Pi}_\ell^u$ and $\bar{\Pi}_\ell^b$ appear as sinks in the energy budgets of large scales $> \ell$ and as sources in the energy budgets of small scales $< \ell$ (Aluie 2017).

The term $\bar{S}_{ij} \bar{B}_i \bar{B}_j$ quantifies KE-to-ME conversion at all scales $> \ell$ and appears as a sink in Equation (4) and a source in Equation (5). Bian & Aluie (2019) showed that $\langle \bar{S}_{ij} \bar{B}_i \bar{B}_j \rangle$ ($\langle \dots \rangle$ denotes a spatial average) is a large-scale process, which only operates at the largest scales in the inertial-inductive range

(which was called the “conversion range”) and vanishes at intermediate and small scales in the inertial-inductive range (which was called the “decoupled range”). In the decoupled range, $\langle \overline{\Pi}_\ell^u \rangle$ and $\langle \overline{\Pi}_\ell^b \rangle$ become constant as a function of scale (i.e., scale independent). The observation of constant KE and ME fluxes $\langle \overline{\Pi}_\ell^u \rangle$ and $\langle \overline{\Pi}_\ell^b \rangle$ is important because it indicates separate conservative cascades of each of KE and ME, which arises asymptotically at high Reynolds number regardless of forcing, external magnetic field, and microscopic magnetic Prandtl number.

2.2. Scaling of Turbulent Transport Coefficients

Oftentimes, turbulence is modeled as a diffusive process via effective (or turbulent) transport coefficients. For example, mixing length or eddy-viscosity models represent the subscale stress $\overline{\tau}_\ell$, due to scales $< \ell$, as $\overline{\tau}_{ij} = -2\nu_t^x \overline{S}_{ij}$, where ν_t^x is a turbulent viscosity⁴ (e.g., Pope 2001 and references therein). Similarly, the subscale EMF can be modeled as $\overline{\varepsilon} = -\eta_t^x \overline{\mathbf{J}} + \alpha \overline{\mathbf{B}}$, where the $\eta_t^x \overline{\mathbf{J}}$ term models the subscales as turbulent resistive diffusion (Miesch et al. 2015) and the $\alpha \overline{\mathbf{B}}$ term is the α -effect of dynamo theory (Moffatt 1978). The α -effect is expected to play a role in flows where the driving mechanism is helical. To simplify our analysis and the presentation of our approach, we shall ignore the $\alpha \overline{\mathbf{B}}$ term and assume that the subscale EMF can be modeled solely as ohmic diffusion, $\overline{\varepsilon} = -\eta_t^x \overline{\mathbf{J}}$. Note that $\nu_t^x(\mathbf{x}, t, \ell)$ and $\eta_t^x(\mathbf{x}, t, \ell)$ are generally functions of space \mathbf{x} , length scale ℓ , and time.

The main goal of this paper is extracting the turbulence transport coefficients, ν_t^x and η_t^x , as a function of length scale. However, we do not pursue a phenomenological analysis similar to that of Smagorinsky (1963) or of a mixing length framework (Tennekes & Lumley 1972) in part because we lack a consensus MHD turbulence theory analogous to that of Kolmogorov (1941). To achieve our goal, we shall instead analyze the energy budgets resulting from the eddy-viscosity model. Within our coarse-graining framework, this is equivalent to having the rate of energy cascading to scales smaller than ℓ equal a turbulent dissipation acting on scales $> \ell$:

$$2\nu_t \langle |\overline{\mathbf{S}}_\ell|^2 \rangle \equiv \langle \overline{\Pi}_\ell^u \rangle, \quad (6)$$

$$\eta_t \langle |\overline{\mathbf{J}}_\ell|^2 \rangle \equiv \langle \overline{\Pi}_\ell^b \rangle. \quad (7)$$

These two relations are definitions for ν_t and η_t . Note that unlike in relation $\overline{\tau}_{ij} = -2\nu_t^x \overline{S}_{ij}$, the turbulence transport coefficients in Equations (6)–(7) are defined using scalar quantities $\langle \overline{\Pi}_\ell^u \rangle$, $\langle \overline{\Pi}_\ell^b \rangle$, $\langle |\overline{\mathbf{S}}_\ell|^2 \rangle$, and $\langle |\overline{\mathbf{J}}_\ell|^2 \rangle$. For homogeneous turbulence considered in this study, we rely on spatial averages, $\langle \dots \rangle$, rendering ν_t and η_t independent of location \mathbf{x} but still a function of scale ℓ .

Consistent with the eddy-viscosity hypothesis, Equation (6) (Equation (7)) models the kinetic (magnetic) energy cascading from scales $> \ell$ to smaller scales as effectively being dissipated by a turbulent viscosity (resistivity). From these, we can also

⁴ Strictly speaking, the eddy-viscosity definition is $\overline{\tau}_{ij} = -2\nu_t \overline{S}_{ij}$, where $\overline{\tau}_{ij} = \overline{\tau}_{ij} - \delta_{ij} \overline{\tau}_{kk} / 3$ is the traceless part of the stress. For our incompressible flow analysis here, which is based on the energy flux, this distinction does not matter.

extract a scale-dependent turbulent magnetic Prandtl number,

$$\text{Pr}_t \equiv \nu_t / \eta_t = \frac{\langle \overline{\Pi}_\ell^u \rangle \langle |\overline{\mathbf{J}}_\ell|^2 \rangle}{\langle \overline{\Pi}_\ell^b \rangle \langle 2|\overline{\mathbf{S}}_\ell|^2 \rangle}. \quad (8)$$

What power-law scaling can we expect these turbulent transport coefficients to have? It is possible to relate ν_t and η_t to energy spectra. Indeed, the space-averaged turbulent dissipation can be expressed in terms of energy spectra:

$$\langle \overline{\Pi}_\ell^u \rangle = 2\nu_t \langle |\overline{\mathbf{S}}_\ell|^2 \rangle = 2\nu_t \int_0^k k'^2 E^u(k') dk', \quad (9)$$

$$\langle \overline{\Pi}_\ell^b \rangle = \eta_t \langle |\overline{\mathbf{J}}_\ell|^2 \rangle = 2\eta_t \int_0^k k'^2 E^b(k') dk', \quad (10)$$

where $E^u(k)$ ($E^b(k)$) is the kinetic (magnetic) energy spectrum with (dimensionless) wavenumber $k = L/\ell$ for a periodic domain of size L .

The scaling of spectra in turn is related to the scaling of velocity and magnetic field increments (Aluie 2017)

$$\delta u(\ell) \propto \ell^{\sigma_u}, \quad \delta B(\ell) \propto \ell^{\sigma_b}, \quad (11)$$

where the increment $\delta f(x; \ell) = f(x + \ell) - f(x)$ (see details in Eyink 2005; Aluie & Eyink 2010; Aluie 2017). From Equation (11), the kinetic and magnetic energy spectra scale as

$$E^u(k) \propto k^{-2\sigma_u-1}, \quad E^b(k) \propto k^{-2\sigma_b-1}. \quad (12)$$

The relation between increments and spectra does not make any assumptions about the specific exponent values, only that they are $\sigma_{u,b} < 1$ (Sadek & Aluie 2018). Scaling exponents σ_u and σ_b are a measure of smoothness of the velocity and magnetic fields, respectively (see Figure 1 and related discussion in Aluie 2017). A value of $\sigma = 1$ indicates that the field is very smooth (e.g., of a laminar flow) with a spectrum decaying as k^{-3} or steeper. Canonical hydrodynamic turbulence has intermediate smoothness, with $\sigma_u = 1/3$ according to Kolmogorov (1941, hereafter K41). The larger the value of σ , the smoother is the field.

For sufficiently high-Reynolds-number flows, Bian & Aluie (2019) showed that each of $\langle \overline{\Pi}_\ell^u \rangle$ and $\langle \overline{\Pi}_\ell^b \rangle$ becomes constant, independent of scale in the decoupled range. From definitions given by Equations (6)–(8), and considering the scaling relations discussed above, we can infer that the turbulent transport coefficients vary with scale as follows:

$$\nu_t \propto k^{-2(1-\sigma_u)}, \quad \eta_t \propto k^{-2(1-\sigma_b)}, \quad \text{Pr}_t \propto k^{-2(\sigma_b-\sigma_u)}, \quad (13)$$

for scales k in the decoupled range. It is possible to obtain the scaling relations in Equation (13) from either the scaling of spectra in Equations (9)–(10), or the scaling of coarse-grained strain and current, $|\overline{\mathbf{S}}_\ell| \sim \delta u(\ell)/\ell$ and $|\overline{\mathbf{J}}_\ell| \sim \delta B(\ell)/\ell$ (Eyink et al. 2013; Aluie 2017). Equation (13) highlights that Pr_t is independent of scale only if $\sigma_u = \sigma_b$.

Regardless of the specific value, and consistent with existing MHD turbulence phenomenologies, we expect that $\sigma_{u,b} < 1$. Indeed, a $\sigma_{u,b} \geq 1$ would correspond to a smooth flow that is inconsistent with the qualitative expectation of a “rough” or “fractal” turbulent flow. Therefore, relations (13) indicate that ν_t and η_t decay as $\ell \rightarrow 0$ (or $k \rightarrow \infty$). This is consistent with physical expectations because the “eddies” affecting the turbulent transport become weaker at smaller scales, yielding smaller transport coefficients.

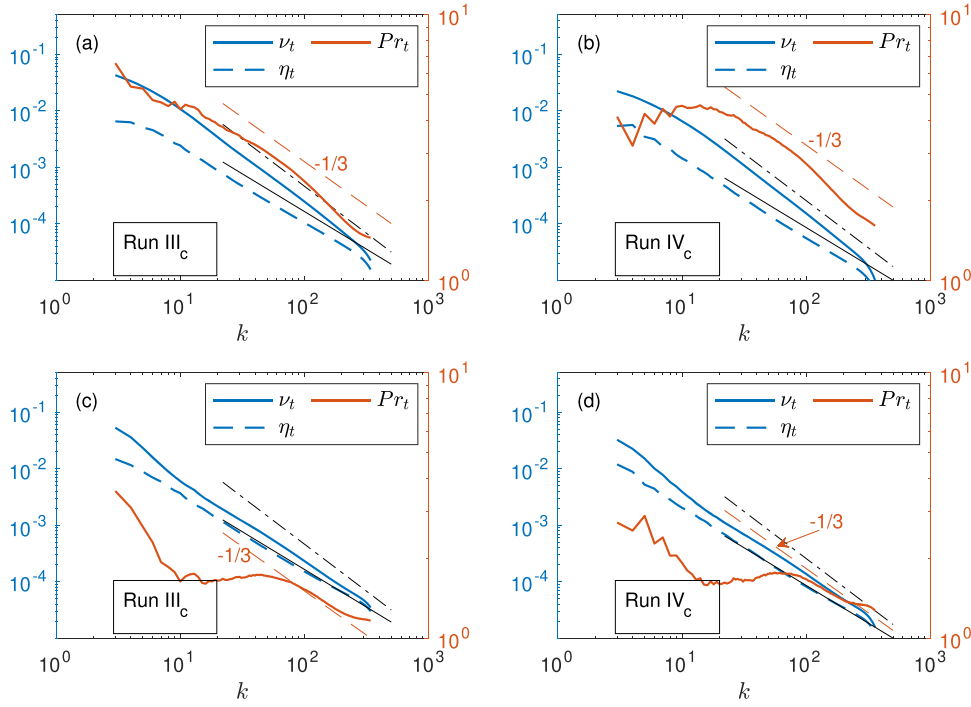


Figure 1. Panels (a)–(b) show ν_t , η_t , and Pr_t calculated using their respective definitions in Equations (6)–(8), at different scales $k = L/\ell$. Panels (c)–(d) show an alternate calculation of ν_t and η_t from Equations (17)–(18). We use the highest-resolution runs of Run III and IV (Taylor–Green forcing) in Table 1. Three reference lines with a slope of $-1/3$, $-5/3$ (black dashed–dotted), and $-4/3$ (black solid) are added. Note the reference line of $-1/3$ and Pr_t use the right y-axis, while others use the left y-axis. Scales $< \ell_d$ are not shown. Simulations with helical forcing are shown in Figure 7 in Appendix.

We highlight a technical, albeit important, aspect of scaling relations in Equation (13). Our coefficients seem to scale with the inverse of coarse-grained strain and current magnitudes, $\nu_t \sim |\bar{\mathbf{S}}_\ell|^{-2} \sim \ell^{2-2\sigma_u}$ and $\eta_t \sim |\bar{\mathbf{J}}_\ell|^{-2} \sim \ell^{2-2\sigma_b}$, but do not appear to depend on the subscale stress and EMF, $\bar{\boldsymbol{\tau}}_\ell$ and $\bar{\boldsymbol{\varepsilon}}_\ell$, respectively. At face value, this result seems counterintuitive wherein $\sigma \rightarrow 1$ associated with smoother fields and weaker “eddies” lead to an increase rather than a drop in the turbulent coefficient values in Equation (13). However, a key assumption to arrive at the relations in Equation (13) is that fluxes $\langle \bar{\Pi}_\ell^u \rangle$ and $\langle \bar{\Pi}_\ell^b \rangle$ are constant, independent of scale. For scale-independent fluxes to be established, consistent with a persistent cascade to arbitrarily small scales (in the $\text{Re} \rightarrow \infty$ limit), σ_u and σ_b have to take on fixed values that are yet to be determined and agreed upon by the community. If $\sigma_{u,b}$ were to be somehow increased above those values, the cascade would shut down (fluxes would decay with k) before carrying the energy all the way to dissipation scales (Aluie 2017). For scale-dependent fluxes, the relations in Equation (13) have to be modified to also include the scaling of $\langle \bar{\Pi}_\ell^u \rangle$ and $\langle \bar{\Pi}_\ell^b \rangle$ (see Aluie 2017 for details).

To infer the scaling of turbulence transport coefficients, the approach we adopt in this paper circumvents using values of σ_u and σ_b (in the asymptotic $\text{Re} \rightarrow \infty$ limit) from a specific MHD phenomenon—whether it exists or not—by relying on results from Bian & Aluie (2019) of scale-independent fluxes $\langle \bar{\Pi}_\ell^u \rangle$ and $\langle \bar{\Pi}_\ell^b \rangle$.

Under the *K41* scaling $\sigma_u = 1/3$ (Kolmogorov 1941), our scaling of $\nu_t \propto \ell^{2-2\sigma_u} \propto \ell^{4/3}$ is equivalent to that from mixing length theory, $\nu_t = \ell^2 |\bar{\mathbf{S}}| \propto \ell^{\sigma_u+1} \propto \ell^{4/3}$ (Smagorinsky 1963). Our analysis is also compatible with different scaling theories and observations in MHD turbulence (Iroshnikov 1963; Kraichnan 1965; Goldreich & Sridhar 1995; Boldyrev 2005, 2006; Boldyrev & Perez 2009; Boldyrev et al. 2011). For example, solar wind

observations (Podesta et al. 2007; Borovsky 2012) suggest that $E^u(k) \sim k^{-3/2}$ for the kinetic energy spectrum, corresponding to $\delta u(\ell) \sim \ell^{1/4}$, and $E^b(k) \sim k^{-5/3}$ for the magnetic energy spectrum, corresponding to $\delta B(\ell) \sim \ell^{1/3}$, yielding

$$\nu_t \sim k^{-3/2}, \eta_t \sim k^{-4/3}, Pr_t \sim k^{-1/6}, \quad (14)$$

for k in the decoupled scale range.

2.3. Alternate Measure of the Coefficients

Instead of analyzing the energy budgets to determine ν_t , η_t , Pr_t , and their scaling, we can alternatively focus on the budgets for vorticity and current. Similar to Equations (4)–(5), we can derive the budgets

$$\partial_t \left(\frac{|\bar{\boldsymbol{\omega}}|^2}{2} \right) + \nabla \cdot [\dots] = \dots - \bar{Z}_\ell \quad (15)$$

$$\partial_t \left(\frac{|\bar{\mathbf{J}}|^2}{2} \right) + \nabla \cdot [\dots] = \dots - \bar{Y}_\ell. \quad (16)$$

Here, $\bar{Z}_\ell = \bar{\boldsymbol{\omega}} \cdot \nabla \times (\nabla \cdot \bar{\boldsymbol{\tau}})$ and $\bar{Y}_\ell = -\bar{\mathbf{J}} \cdot \nabla \times \nabla \times \bar{\boldsymbol{\varepsilon}}$ are the only “scale-transfer” terms in the coarse-grained Equations (15)–(16) involving the interaction of subscale terms $\bar{\boldsymbol{\tau}}_\ell$ and $\bar{\boldsymbol{\varepsilon}}_\ell$ with large-scale quantities (here, $\bar{\boldsymbol{\omega}}$ and $\bar{\mathbf{J}}$) to cause transfer across scale ℓ . From the models $\bar{\boldsymbol{\tau}}_\ell = -2\nu_t \bar{\mathbf{S}}_\ell$ and $\bar{\boldsymbol{\varepsilon}}_\ell = -\eta_t \bar{\mathbf{J}}_\ell$, we have alternate definitions for the turbulent transport coefficients:

$$\nu_t \equiv \frac{1}{4} \frac{\langle \bar{Z}_\ell \rangle}{\langle |\nabla \cdot \bar{\mathbf{S}}_\ell|^2 \rangle} \quad (17)$$

$$\eta_t \equiv \frac{\langle \bar{Y}_\ell \rangle}{\langle |\nabla \times \bar{\mathbf{J}}_\ell|^2 \rangle}. \quad (18)$$

Note that unlike energy, vorticity and current density are not ideal invariants and, therefore, do not undergo a cascade in the

manner energy does. Yet, to the extent that ν_t and η_t are able to capture the subscale physics embedded in $\overline{\tau}_\ell$ and $\overline{\varepsilon}_\ell$, it is reasonable to expect that the turbulent transport coefficients are consistent with the budget of any quantity derived from the underlying dynamics.

In Figure 1, we compare ν_t and η_t when calculated from Equations (17)–(18) to those obtained from the energy budgets in Equations (6)–(7). We find that the two definitions yield fairly similar results with slight quantitative differences. This consistency lends support to our approach of using the energy budgets to calculate ν_t and η_t (Equations (6)–(7)) and make inferences about the turbulent diffusion or dissipation of quantities other than energy.

2.4. Implications to Subgrid Modeling

It is almost always the case that astrophysical systems of interest are at sufficiently high Reynolds numbers (both magnetic and hydrodynamic) that it is impossible to simulate the entire dynamic range of scales that exist (Miesch et al. 2015). In practice, most simulations are either explicit or implicit LES, resolving only the large-scale dynamics (Meneveau & Katz 2000). The former includes explicit terms in the equations being solved that model the unresolved subgrid physics, whereas the latter relies on the numerical scheme to act as a de facto model for such missing physics. Our analysis here can offer guidance for tuning the turbulent coefficients when conducting explicit LESs using eddy diffusivity models. It can also offer us insight into whether relying on a similar scheme and grid for simulating both the momentum and magnetic fields is justified.

In the inertial-inductive range, using Equation (6), $|\overline{\mathcal{S}}_\ell| \sim \delta u(\ell)/\ell$, and the ansatz (Aluie 2017)

$$\delta u(\ell) \propto u_{\text{rms}} \left(\frac{\ell}{L} \right)^{\sigma_u}, \quad (19)$$

where $u_{\text{rms}} = \langle |\mathbf{u}|^2 \rangle^{1/2}$ and L is a characteristic large scale such as the integral scale or that of the domain, and we ignore intermittency corrections. We then have

$$\nu_t = \frac{\langle \overline{\Pi}_\ell^u \rangle}{(2|\overline{\mathcal{S}}_\ell|^2)} \sim \frac{\langle \overline{\Pi}_\ell^u \rangle \ell^2}{|\delta u|^2} \sim \frac{\langle \overline{\Pi}_\ell^u \rangle}{u_{\text{rms}}^2/L^2} \left(\frac{\ell}{L} \right)^{2-2\sigma_u}. \quad (20)$$

In an LES with grid spacing Δx , the turbulent viscosity accounting for subgrid scales should be evaluated at a coarse-graining scale $\ell_c = L/k_c$ proportional to Δx (Pope 2001), where $k_c = L/\ell_c$ is a dimensionless cutoff wavenumber:

$$\nu_t(k = k_c) = \frac{\langle \overline{\Pi}_\ell^u \rangle}{2C_u^2 u_{\text{rms}}^2/L^2} \left(\frac{1}{k_c} \right)^{2-2\sigma_u}, \quad (21)$$

for $(\ell_\nu, \ell_\eta) \ll \ell_c \ll L$, where the dimensionless constant C_u is defined as the proportionality factor of the relation

$$\langle |\overline{\mathcal{S}}_\ell|^2 \rangle^{1/2} = C_u \frac{u_{\text{rms}}}{L} \left(\frac{\ell}{L} \right)^{\sigma_u-1}. \quad (22)$$

Figure 6 in Appendix B shows that C_u is indeed a proportionality constant that is scale independent within the decoupled range, taking on values from 2 to 5 in various simulated flows.

Table 1
Simulation Parameters

Run	Forcing	k_f	Pr_m	$ B_0 /B_k^{\text{max}}$	N_{max}^3
I	ABC	2	1	0	1024^3
II	ABC	2	1	10	1024^3
III	TG	1	1	0	1024^3
IV	TG	1	2	0	1024^3
IV($\text{Pr}_m = 0.1$)	TG	1	0.1	0	512^3
IV($\text{Pr}_m = 5$)	TG	1	5	0	512^3
IV($\text{Pr}_m = 10$)	TG	1	10	0	512^3
V	ABC	2	1	2	2048^3

Note. ABC (helical) and Taylor–Green (TG; nonhelical) forcing are applied at wavenumber k_f . $B_k^{\text{max}} = \sqrt{\max_k [E^b(k)]}$ is at the magnetic spectrum’s $[E^b(k)]$ peak. Each simulation set includes runs with the same parameters except grid resolution (Reynolds numbers). N_{max}^3 denotes the highest resolution in each set. Subscripts a, b, c, and d denote resolutions of 256^3 , 512^3 , 1024^3 , and 2048^3 , respectively. More details are given in Table 2 in Appendix B.

Similarly, the turbulent resistivity at the cutoff wavenumber is

$$\eta_t(k = k_c) = \frac{\langle \overline{\Pi}_\ell^b \rangle}{C_b^2 B_{\text{rms}}^2/L^2} \left(\frac{1}{k_c} \right)^{2-2\sigma_b}, \quad (23)$$

where $B_{\text{rms}} = \langle |B - B_0|^2 \rangle^{1/2}$ (B_0 is the uniform external magnetic field), and the dimensionless constant C_b is defined as

$$\langle |\overline{\mathcal{J}}_\ell|^2 \rangle^{1/2} = C_b \frac{B_{\text{rms}}}{L} \left(\frac{\ell}{L} \right)^{\sigma_b-1}. \quad (24)$$

Figure 6 in Appendix B shows that C_b is indeed a proportionality constant that is scale independent within the decoupled range, taking on values from 10 to 15 in various simulated flows.

If the grid is sufficiently fine to resolve some of the scales in the decoupled range, then Equations (21) and (23) simplify to

$$\nu_t(k = k_c) = \frac{\varepsilon_u}{2C_u^2 u_{\text{rms}}^2/L^2} \left(\frac{1}{k_c} \right)^{2-2\sigma_u}, \quad (25)$$

$$\eta_t(k = k_c) = \frac{\varepsilon_b}{C_b^2 B_{\text{rms}}^2/L^2} \left(\frac{1}{k_c} \right)^{2-2\sigma_b}, \quad (26)$$

with scale-independent fluxes $\langle \overline{\Pi}_\ell^u \rangle = \varepsilon_u$ and $\langle \overline{\Pi}_\ell^b \rangle = \varepsilon_b$. These are the KE and ME cascade rates, which were found by Bian & Aluie (2019) to reach equipartition in the decoupled range, $\varepsilon_u = \varepsilon_b = \varepsilon/2$, half the total energy cascade rate, ε .

Equations (21) and (23) (and Equations (25) and (26)) connect the scaling of turbulent transport coefficients with the scaling of velocity and magnetic spectra and are compatible with different MHD scaling theories. For example, if $E^u(k) \sim k^{-5/3}$ (corresponding to $\delta u(\ell) \sim \ell^{1/3}$) as in the theory by Goldreich & Sridhar (1995), Equation (21) reduces to the turbulent viscosity model of Verma (2001a) derived from an RG analysis (see also Verma & Kumar 2004).

3. Numerical Results

We conduct pseudo-spectral direct numerical simulations (DNS) of MHD turbulence using hyperdiffusion with grid resolutions up to 2048^3 . Simulation parameters are summarized in Table 1 (see details in Table 2 in Appendix B). To discern trends in the high-Re asymptotic limit, each set of simulations

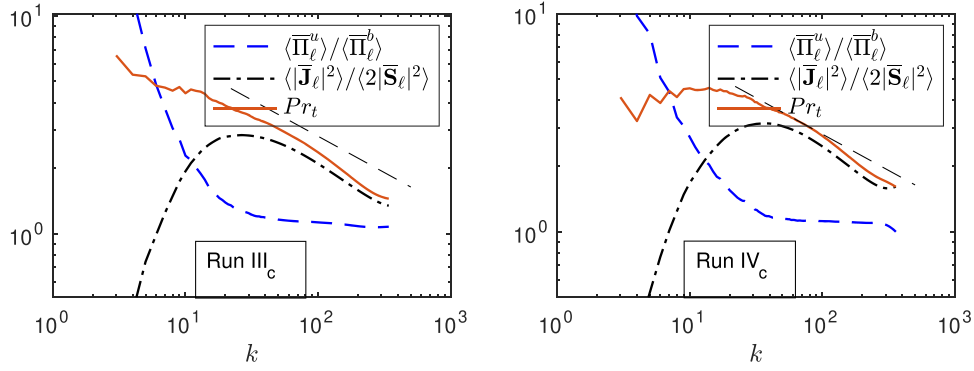


Figure 2. Plots showing Pr_t and its two components $\langle \bar{\Pi}_\ell^u \rangle / \langle \bar{\Pi}_\ell^b \rangle$ and $\langle |\bar{\mathbf{J}}_\ell|^2 \rangle / \langle 2|\bar{\mathbf{S}}_\ell|^2 \rangle$ at the highest resolutions of Runs III and IV (Taylor–Green forcing) in Table 1. A reference line with a slope of $-1/3$ (black dashed) is added. The plots show that $\langle \bar{\Pi}_\ell^u \rangle / \langle \bar{\Pi}_\ell^b \rangle$ approaches a constant in the decoupled range. Simulations with helical forcing are shown in Figure 8 in Appendix C.

is run under the same parameters but at different grid resolutions (Reynolds numbers). Our flows are driven with either nonhelical forcing (Runs III and IV) or helical forcing (Runs I, II, and IV). Because we do not account for the α -effect when modeling the turbulent EMF, $\bar{\epsilon}$, which may be important in helically driven flows, we focus on results from Runs III and IV in the main text while those driven with helical forcing (Runs I, II, and IV) are shown in Appendix B for completeness. We note that all simulations yield remarkably similar results, regardless of the type of forcing.

In our simulations, we observe a scaling of $E^u(k) \sim k^{-4/3}$ in Runs I_c, III_c, and IV_c, and $E^u(k) \sim k^{-3/2}$ in Runs II_c and V_d (see Figures 10 and 11 in Appendix C), corresponding to scaling exponents of $\sigma_u = 1/6$ and $\sigma_u = 1/4$, respectively. $E^b(k) \sim k^{-5/3}$ in all runs (at the highest resolution), corresponding to scaling exponents of $\sigma_b = 1/3$. The $E^b(k)$ scaling is consistent with that reported in solar wind studies (Podesta et al. 2007; Borovsky 2012). The $E^u(k) \sim k^{-4/3}$ scaling is consistent with that reported by Grete et al. (2020b) using the code K-Athena (Grete et al. 2020; Stone et al. 2020) and is slightly shallower than the $k^{-3/2}$ reported in other studies (Haugen et al. 2004; Borovsky 2012), possibly due to the pronounced bottleneck effect from using hyperdiffusion (Frisch et al. 2008).

Without placing too much emphasis on the specific values of σ_u and σ_b for now, we wish to check if the scaling we derived in Equation (13) is consistent with the σ_u and σ_b we observe in our simulations. Figures 1(a) and (b) (also Figure 7 in Appendix B) show the effective transport coefficients ν_t , η_t , and Pr_t as a function of scale calculated using their respective definitions in Equations (6)–(8). We can see that $\nu_t(k) \sim k^{-5/3}$ (or $\sim k^{-3/2}$) and $\eta_t(k) \sim k^{-4/3}$, consistent with Equation (13) when $\sigma_u = 1/6$ (or $\sigma_u = 1/4$) and $\sigma_b = 1/3$ as in our simulations. Moreover, we see in Figures 1(a) and (b) (and Figure 7 in Appendix B) that $Pr_t(k) \sim k^{-1/3}$ (or $\sim k^{-1/6}$), which is also consistent with the derived scaling in Equation (13) with $\sigma_u = 1/6$ (or $\sigma_u = 1/4$) and $\sigma_b = 1/3$ in our simulated flows. Panels (c)–(d) in Figure 1 also show ν_t , η_t , and Pr_t but calculated from Equations (17)–(18). Turbulent resistivity is very similar to that in Figures 1(a) and (b) with an $\eta_t \sim k^{-4/3}$ scaling, whereas ν_t has a scaling that is slightly shallower than that in Figures 1(a) and (b). Because $Pr_t = \nu_t/\eta_t$, it is sensitive to slight changes in the scaling with $Pr_t \sim k^{-1/3}$ only over the decoupled range $k \in [50, 200]$ but not for smaller k .

Qualitatively, the scalings of transport coefficients in Figures 1(c) and (d) are consistent with those in Figures 1(a)

and (b), generally increasing at larger scales. We believe that this agreement between the different definitions of transport coefficients will be enhanced as the dynamic range increases and more definitive power-law scalings emerge. Indeed, we will present evidence below that the dynamic range in simulations that are possible today, including ours here, does not yet have a converged power-law scaling.

The scaling of $\eta_t \sim k^{-4/3}$ agrees with our Equation (14) applicable to the solar wind, as does $\nu_t \sim k^{-3/2}$ from Runs II_c and V_d. The scaling of $\nu_t \sim k^{-5/3}$ in Runs I_c, III_c, and IV_c decays faster than the $k^{-3/2}$ in Equation (14) because $\sigma_u < 1/4$ in those simulations, associated with a shallower spectrum. This may be attributed to the bottleneck effect from hyperviscosity (Frisch et al. 2008), which produces a pileup at the small scales (see the spectra in Figure 10 of Appendix).

Figures 1(a) and (b) also show a Pr_t larger than unity in the inertial-inductive range, decreasing to $Pr_t \approx 1$ to 2 at the smallest inertial-inductive scales ℓ_d in all cases (see also Table 3 in Appendix B), where ℓ_d is defined as the scale where $\langle \bar{\Pi}_\ell^u + \bar{\Pi}_\ell^b \rangle = \nu \langle |\nabla \bar{\mathbf{u}}|^2 \rangle + \eta \langle |\nabla \bar{\mathbf{B}}|^2 \rangle$. For non-unity Pr_m , $\ell_d \equiv \max(\ell_\nu, \ell_\eta)$. ℓ_ν and ℓ_η are defined as scales where $\langle \bar{\Pi}_\ell^u \rangle = \nu \langle |\nabla \bar{\mathbf{u}}|^2 \rangle$ and $\langle \bar{\Pi}_\ell^b \rangle = \eta \langle |\nabla \bar{\mathbf{B}}|^2 \rangle$.

Figure 2 (and Figure 8 in Appendix C) shows ratios $\langle \bar{\Pi}_\ell^u \rangle / \langle \bar{\Pi}_\ell^b \rangle$ and $\langle |\bar{\mathbf{J}}_\ell|^2 \rangle / \langle 2|\bar{\mathbf{S}}_\ell|^2 \rangle$, the product of which yields Pr_t in Equation (8). $\langle \bar{\Pi}_\ell^u \rangle / \langle \bar{\Pi}_\ell^b \rangle$ becomes constant in the decoupled range due to the conservative (constant) KE and ME cascades in this range. $\langle |\bar{\mathbf{J}}_\ell|^2 \rangle / \langle 2|\bar{\mathbf{S}}_\ell|^2 \rangle$ is equal to $\int_0^k k'^2 E^b(k') dk' / \int_0^k k'^2 E^u(k') dk'$. The ratio $\langle |\bar{\mathbf{J}}_\ell|^2 \rangle / \langle 2|\bar{\mathbf{S}}_\ell|^2 \rangle$ increases because $E^b(k) < E^u(k)$ at forcing scales (forcing in velocity field) but $E^b(k)$ catches up and exceeds $E^u(k)$ at larger k . The ratio $\langle |\bar{\mathbf{J}}_\ell|^2 \rangle / \langle 2|\bar{\mathbf{S}}_\ell|^2 \rangle$ decays after reaching a peak because (1) each of $\bar{\mathbf{J}}_\ell$ and $\bar{\mathbf{S}}_\ell$ is dominated by the largest wavenumbers below the cutoff $k < L/\ell$, and (2) $E^u(k)$ is shallower than $E^b(k)$ at high k in the inertial-inductive range, making $|\bar{\mathbf{S}}_\ell|^2$ grow faster than $|\bar{\mathbf{J}}_\ell|^2$ as $\ell \rightarrow 0$.

4. Discussion

We now provide the physical explanation for why Pr_t seems to increase at larger scales and discuss whether or not this trend is expected to persist for an arbitrarily wide dynamical range ($Re \rightarrow \infty$). As we have mentioned above, σ^u and σ^b are a measure of the velocity and magnetic fields' smoothness, respectively (Aluie 2017). If $\sigma_u < \sigma_b$ (corresponding to a shallower scaling of $E^u(k)$ relative to $E^b(k)$) as in our simulations and many other

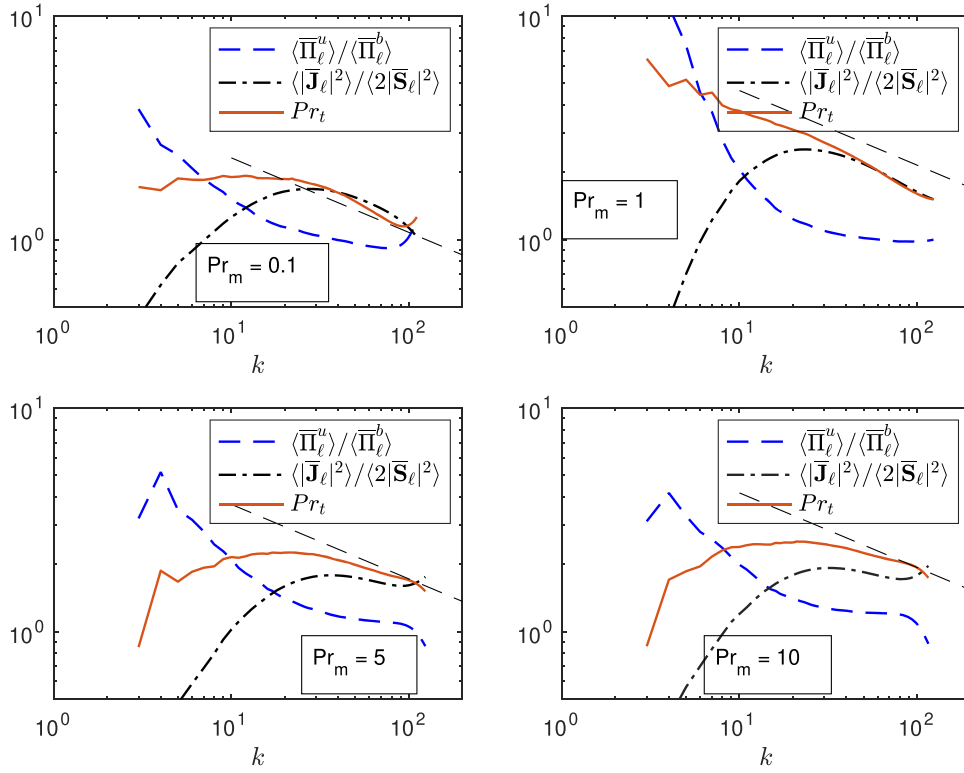


Figure 3. Plots showing Pr_t and its two components $\langle \bar{\Pi}_\ell^u \rangle / \langle \bar{\Pi}_\ell^b \rangle$ and $\langle |\bar{\mathbf{J}}_\ell|^2 \rangle / \langle 2|\bar{\mathbf{S}}_\ell|^2 \rangle$ using unity ($Pr_m = 1$) and non-unity microscopic Prandtl numbers ($Pr_m = 0.1, 5, 10$) on a 512^3 grid. See parameters in Table 1. A reference line with a slope of $-1/3$ (black dashed line) is added.

independent reports from solar wind observations and simulations (e.g., Podesta et al. 2007; Mininni & Pouquet 2009; Borovsky 2012; Grappin et al. 2016), then the velocity field is rougher than the magnetic field. This implies that small-scale velocity “eddies” have a higher proportion of the overall kinetic energy compared to the proportion small-scale magnetic “eddies” contribute to the overall magnetic energy (i.e., $\frac{\text{small-scale KE}}{\text{total KE}} > \frac{\text{small-scale ME}}{\text{total ME}}$). Note that the latter statement is not based on comparing $E^u(k)$ to $E^b(k)$ at high k in absolute terms, where we see $E^b(k) \gtrsim E^u(k)$. Rather, it is based on the strength of “eddies” relative to the overall velocity or magnetic field, respectively.

The coarse-grained strain and current, $\bar{\mathbf{S}}_\ell$ and $\bar{\mathbf{J}}_\ell$, are cumulative quantities, i.e., they include the contribution from all scales larger than ℓ , for any ℓ . It follows from the above paragraph that as the coarse-graining ℓ is made smaller, the relative contribution from scales near ℓ to $|\bar{\mathbf{S}}_\ell|^2$ is more significant than that to $|\bar{\mathbf{J}}_\ell|^2$. From the definition of Pr_t in Equation (8) and with $\langle \bar{\Pi}_\ell^u \rangle / \langle \bar{\Pi}_\ell^b \rangle$ being scale independent in the decoupled range, we have $Pr_t \propto \langle |\bar{\mathbf{J}}_\ell|^2 \rangle / \langle 2|\bar{\mathbf{S}}_\ell|^2 \rangle$ in the decoupled range. Clear evidence of this is shown in Figure 2 (and Figures 3 and 8). As ℓ decreases (or k increases), both $|\bar{\mathbf{S}}_\ell|^2$ and $|\bar{\mathbf{J}}_\ell|^2$ increase because contributions from $< \ell$ are included. However, due to the larger roughness of the velocity field, the increase in $|\bar{\mathbf{S}}_\ell|^2$ is more pronounced than that in $|\bar{\mathbf{J}}_\ell|^2$, leading to a decrease in the ratio $\langle |\bar{\mathbf{J}}_\ell|^2 \rangle / \langle 2|\bar{\mathbf{S}}_\ell|^2 \rangle$. This explains why Pr_t seems to decrease with larger k over the decoupled range (range over which each of $\langle \bar{\Pi}_\ell^u \rangle$ and $\langle \bar{\Pi}_\ell^b \rangle$ is scale independent).

In the conversion range over which $\langle \bar{\Pi}_\ell^u \rangle$ and $\langle \bar{\Pi}_\ell^b \rangle$ are still varying with ℓ , the scaling of Pr_t depends on both $\langle \bar{\Pi}_\ell^u \rangle / \langle \bar{\Pi}_\ell^b \rangle$ and $\langle |\bar{\mathbf{J}}_\ell|^2 \rangle / \langle 2|\bar{\mathbf{S}}_\ell|^2 \rangle$. On the one hand, $\langle \bar{\Pi}_\ell^u \rangle / \langle \bar{\Pi}_\ell^b \rangle > 1$ because energy is input into the velocity field at the largest scales and

more kinetic energy is cascading compared to magnetic energy, such that $\langle \bar{\Pi}_\ell^u \rangle / \langle \bar{\Pi}_\ell^b \rangle \rightarrow \infty$ as $\ell \rightarrow \ell_f$ approaches the forcing scale ℓ_f . On the other hand, we have the ratio $\langle |\bar{\mathbf{J}}_\ell|^2 \rangle / \langle 2|\bar{\mathbf{S}}_\ell|^2 \rangle$ decreasing in that limit of $\ell \rightarrow \ell_f$ because the strain becomes relatively stronger at the forced scales. From Figure 2, we find that in our simulated flows, the Pr_t scaling over the conversion range either decaying weakly or flat as k increases. Because the conversion range is limited in extent and does not increase with an increasing dynamic range (Bian & Aluie 2019), it is not very meaningful to discuss a scaling of Pr_t over this range.

Crude estimates of the competition between large-scale magnetic flux advection and large-scale magnetic flux diffusion in accretion disks require $Pr_t(R/H) > 1$ (where H is the disk scale height and R is the disk radius) for the former to be competitive with the latter in the disk interior (Lubow et al. 1994; Blackman & Nauman 2015).⁵ That we find values of $Pr_t > 1$ means that large-scale MHD flow may be more efficient at advecting large-scale magnetic flux while shedding angular momentum outward (via ν_t) than would be the case for $Pr_t \leq 1$. That said, pinning down the exact implications are difficult given the additional dependence of disk physics on stratification with the possibility of flux advection in surface layers (e.g., Lovelace et al. 2009; Zhu & Stone 2018).

4.1. Pr_t Scaling under Different Flow Conditions

We have tested the scaling of Pr_t under different microscopic Pr_m flow conditions. We remind the reader that our results here pertain to the decoupled range, which is within the inertial-inductive range. These scales are immune from the direct

⁵ The turbulent Prandtl number used in Lubow et al. (1994) is the inverse of Pr_t .

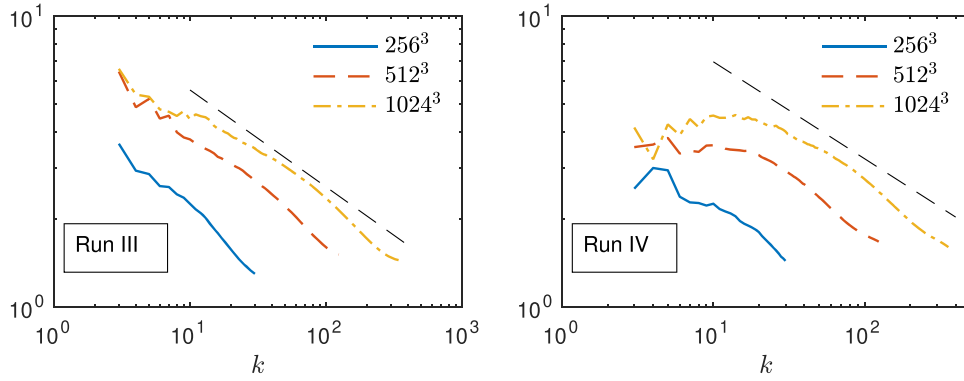


Figure 4. Plots showing Pr_t at different Reynolds numbers (grid resolution) of Runs III and IV (Taylor–Green forcing) in Table 1. A reference line with a slope of $-1/3$ (black dashed) is added. Simulations with helical forcing are shown in Figure 9 in Appendix C.

influence of both resistivity and viscosity. We do not expect our results here (and those of Bian & Aluie 2019 upon which this analysis is based) to hold in the viscous-inductive (Batchelor) range at high Pr_m or in the inertial-resistive range at low Pr_m . From practical modeling considerations, such as when simulating a galactic accretion disk at global scales, grid-resolution constraints render it virtually impossible to have $\Delta x \sim \ell$ within the viscous-inductive range. Therefore, the restriction of our analysis to inertial-inductive scales is still pertinent to modeling as well as being of theoretical import.

Figures 1(a) and (b) show the case (Run IV) of $\text{Pr}_m = 2$, where we find a scaling of Pr_t similar to the case of unity microscopic Pr_m . We also conduct simulations (Table 1) at $\text{Pr}_m = 0.1, 5$, and 10 , albeit at a lower resolution of 512^3 due to the computational overhead required by non-unity Pr_m . Figure 3 shows that the scale dependence of Pr_t is consistent with that of unity- Pr_m runs, although the scaling is not as clear. Due to the lower resolution, the decoupled range is barely established in the non-unity Pr_m cases. Non-unity Pr_m simulations require even larger Reynolds numbers to achieve a significant decoupled range and still make an allowance for a viscous-inductive or an inertial-resistive range of scales. This is beyond our computing capability for this work.

Our results also suggest that within the limited dynamic range of our simulations, increasing the external B -field strength from 0 (Run I) to 2 (Run V) to 10 (Run II) seems to change the Pr_t scaling slightly from $k^{-1/3}$ to $k^{-1/6}$ due to σ_u increasing from $1/6$ to $1/4$ (see Figure 7 in Appendix B). However, we do not believe this trend will persist at asymptotically high-Re as we discuss in the following subsection. We also note that our analysis here does not distinguish the anisotropy in turbulent transport. Our effective transport coefficients in this paper are isotropic even though the underlying turbulent flow may be anisotropic such as in Runs II and V (see Figure 5 in Appendix B). We hope this work is extended to anisotropic turbulent transport in future studies.

4.2. Pr_t Scaling at Asymptotically High Re

Can we expect the scaling of Pr_t in Figures 1(a) and (b), which is in support of our relations in Equation (13), to extrapolate to the wide dynamical ranges (high Re) that exist in many astrophysical systems of interest?

Figure 4 (and Figure 9 in Appendix C) examines the scaling of $\text{Pr}_t(k)$ at different Reynolds numbers. Each panel shows results from a suite of simulations under the same parameters

except for Re (or grid resolution). The plots show that $\text{Pr}_t(k)$ takes on a value between 1 and 2 at the smallest scales within the inertial-inductive range, regardless of Re (also Figure 16 and Table 3 in Appendix C). These scales near ℓ_d are bordering the dissipation range. The reason $\text{Pr}_t(k \approx L/\ell_d) \approx 1-2$ can be understood from the definition in Equation (8) of $\text{Pr}_t = (\langle \overline{\Pi}_\ell^u \rangle / \langle \overline{\Pi}_\ell^b \rangle) (\langle |\overline{\mathcal{J}}_\ell|^2 \rangle / \langle 2|\overline{\mathcal{S}}_\ell|^2 \rangle)$. Due to the equipartition of the cascades in the decoupled range, we have $\langle \overline{\Pi}_\ell^u \rangle / \langle \overline{\Pi}_\ell^b \rangle \approx 1$, whereas $\langle |\overline{\mathcal{J}}_\ell|^2 \rangle / \langle 2|\overline{\mathcal{S}}_\ell|^2 \rangle \approx 1$ to 2, as is clear from Figure 2 (and Figures 3 and 8). The latter can also be inferred from comparing the spectra $E^u(k')$ and $E^b(k')$ in Figures 10–11 via Equations (9)–(10).

Based on these observations, it is physically reasonable to assume that for a sufficiently wide dynamical range (or large Re), $\langle |\overline{\mathcal{J}}_{\ell_d}|^2 \rangle / \langle 2|\overline{\mathcal{S}}_{\ell_d}|^2 \rangle$ converges to a constant when $\ell \approx \ell_d$ (or $k \approx k_d$), independent of the dynamical range extent (i.e., independent of Re). That is, the ratio $\langle |\overline{\mathcal{J}}_{\ell_d}|^2 \rangle / \langle 2|\overline{\mathcal{S}}_{\ell_d}|^2 \rangle$ has the same value under successive refinements of the grid. This effectively provides us with a conceptual boundary condition on $\text{Pr}_t(k)$ at those smallest scales $k \approx k_d$.

These logical considerations, when combined with the scaling $\text{Pr}_t(k) \sim k^{-2(\sigma_b - \sigma_u)}$ in Equation (13) (with empirical support in Figures 1(a), 1(b), and 7), may lead us at face value to the uncomfortable conclusion that at any fixed k in the inertial-inductive range, $\text{Pr}_t(k)$ will keep increasing with increasing Re (or higher resolution) as Figure 4 (and Figure 9 in Appendix C) seems to indicate. That is unless the MHD dynamics eventually yields $\sigma_u = \sigma_b$ in this asymptotic limit, i.e., at successively higher-resolution simulations. Indeed, there are indications from Figures 4 and 9 that the $\text{Pr}_t(k)$ sensitivity to Re decreases with increasing Re as we now discuss.

At first glance, Figure 4 seems to indicate that $\text{Pr}_t(k)$ at any fixed wavenumber, e.g., $k = 50$ within the decoupled range, $\text{Pr}_t(k = 50)$, increases with increasing resolution. Yet, as we shall now argue, Figure 4 highlights how certain metrics such as Pr_t in our simulations, which are very high resolution by today’s standards, are still not fully converged to the high-Re limit. From the definition of Pr_t in Equation (8), this increase can only be due to an increase of the cascade ratios, $\langle \overline{\Pi}_\ell^u \rangle / \langle \overline{\Pi}_\ell^b \rangle$, or the current-to-strain ratio, $\langle |\overline{\mathcal{J}}_\ell|^2 \rangle / \langle 2|\overline{\mathcal{S}}_\ell|^2 \rangle$, or both. We find in Figure 15 that the latter accounts for most of this increase. Figure 15 suggests that the cascade ratio $\langle \overline{\Pi}_\ell^u \rangle / \langle \overline{\Pi}_\ell^b \rangle$ is fairly converged with resolution in our largest simulations at $\ell = L/50$. Physically, we expect $\langle |\overline{\mathcal{J}}_\ell|^2 \rangle / \langle 2|\overline{\mathcal{S}}_\ell|^2 \rangle$ to also converge

because the ratio depends on the strain and current (or equivalently, the spectra) at scales larger than $L/50$. These should not remain sensitive to the smallest scales in a simulation once a sufficiently high resolution has been achieved. Figure 15 in Appendix C indicates that the high resolution of our simulations is still not sufficient for the convergence of these quantities ($\langle 2|\bar{S}_\ell|^2 \rangle$ and $\langle |\bar{J}_\ell|^2 \rangle$). Ignoring convergence trends under the guise of “having conducted the highest-resolution simulation to date” can be rife with pitfalls. In general, when analyzing simulations of turbulent flows, it is vitally important to study trends as a function of Reynolds number and check if the phenomenon under study persists and can be extrapolated to the large Reynolds numbers present in nature.

What conclusion on $\text{Pr}_t(k)$ scaling does these convergence considerations lead us to? If we accept that with increasing resolution, $\text{Pr}_t(k_*)$ has to converge to a specific value for any fixed k_* within the inertial-inductive range, and if we also accept that at the smallest scales within the inertial-inductive range $\approx \ell_d$, $\text{Pr}_t(k_d)$ also converges to a constant value, then as the gap between k_* and k_d widens with a wider dynamical range ($k_d \rightarrow \infty$), we must have that $\text{Pr}_t(k) \sim k^{-2(\sigma_b - \sigma_u)} \sim k^0$ approach a k -independent scaling with $\sigma_b = \sigma_u$ in the asymptotic limit $\text{Re} \rightarrow \infty$. Our Figures 4 and 9 lend some support to our assertion as they show that the $\text{Pr}_t(k)$ is converging (but not converged) at the largest scales with increasing resolution.

Such a conclusion would have wide-ranging implications, foremost of all regarding the power-law scaling of spectra in MHD turbulence. However, it is important that our results are further verified by the community under different parameter conditions, e.g., B_0 strength and Pr_m , and perhaps also from higher-resolution simulations.

5. Conclusion

In this paper, we are proposing a somewhat new method to measure turbulent transport coefficients (turbulent viscosity ν_t , resistivity η_t , and magnetic Prandtl number Pr_t) at different scales using the coarse-graining approach. To our knowledge, this is the first determination of Pr_t as a function of length scale. From analyzing the kinetic and magnetic energy cascade rates, we infer power-law scaling in Equation (13) for ν_t , η_t , and Pr_t given our definitions of those transport coefficients. This approach circumvents relying on particular values for the spectral scaling exponents (σ_u and σ_b) from a specific MHD phenomenology—whether it exists or not—by relying on results from Bian & Aluie (2019) of conservative KE and ME cascades. Our analysis here relied on high-resolution DNS under different forcing, external B -field strength, and microphysical Pr_m .

Our DNS results indicate that $\text{Pr}_t \approx 1$ to 2 at the smallest inertial-inductive scales, increasing to $\text{Pr}_t \approx 5$ to 10 at the largest scales. For accretion disks, conservative minimalist estimates for the advection of large-scale vertical magnetic fields to win over turbulent diffusion require $\text{Pr}_t(H/R) > 1$, so that larger values of Pr_t improve the efficacy of flux advection over diffusion (e.g., Lubow et al. 1994). This condition and the direct applicability of our specific results are both textured by detailed disk physics (e.g., Zhu & Stone 2018), including stratification, not studied here.

Nevertheless, based on physical considerations, our analysis suggests that Pr_t has to become scale independent and of order

unity in the decoupled range at sufficiently high Reynolds numbers (or grid resolution) and that the power-law scaling exponents of velocity and magnetic spectra become equal.

If indeed the power-law scaling exponents of velocity and magnetic spectra (σ_u and σ_b) become equal in the $\text{Re} \rightarrow \infty$ limit, it would have wide-ranging implications, foremost of all regarding the power-law scaling of spectra in MHD turbulence (Politano & Pouquet 1998a, 1998b; Aluie 2017). However, as discussed above, our Pr_t scaling is not quite converged, despite showing a converging trend. It is important for our results to be further checked by the community using simulations of higher resolution and for a wider range of parameters, e.g., B_0 strengths and Pr_m values.

Our results also suggest that the presence of a mean B field does not affect Pr_t significantly. However, we only consider Pr_t as a scalar in this study. Lesur & Longaretti (2009) considered an anisotropic turbulent resistivity tensor with an external B field. Under non-unity microphysical Pr_m , our results are consistent with those of $\text{Pr}_m = 1$, although we could not establish a clear decoupled range due to insufficient simulation resolution.

In addition to potential implications for astrophysical systems, our analysis of how ν_t , η_t , and Pr_t vary with length scale provides a practical model for these quantities that does not rely on any particular MHD turbulence phenomenology.

The simulations we conducted here are fairly idealized (incompressible flows in a periodic domain with artificial forcing). We hope that this work offers a path to analyzing more complicated flows because our method can be applied to more realistic simulations such as of global accretion disk flows. For the pursuit of isotropic diffusion coefficients, measuring ν_t and η_t at any length scale from Equations (6) and (7) does not require the existence of an inertial range or even turbulence, even though in the present paper we applied the method to a case of fully developed turbulence. For some applications, we believe that our approach complements existing approaches such as test-field methods (Schrinner et al. 2007; Käpylä et al. 2020) of measuring turbulent transport. These methods involve taking the velocities computed from a numerical simulation and then separately solving for the transport coefficients using an imposed test magnetic field. Traditionally, these have been restricted to the kinematic regime of a weak magnetic field (although see Käpylä et al. 2021).

Finally, our work should not be construed as an endorsement of the “eddy-viscosity/resistivity” model wherein turbulent processes $\bar{\tau}_\ell$ and $\bar{\varepsilon}_\ell$ representing scales $< \ell$ are modeled as purely diffusive. Our approach can be extended to models in which transport is not entirely diffusive, such as those that include the helical α -effect.

This research was funded by DOE FES grants DE-SC0014318 and DE-SC0020229. Partial funding for this research was provided by the Center for Matter at Atomic Pressures (CMAP), a National Science Foundation (NSF) Physics Frontier Center, under award PHY-2020249. H.A. was also supported by NASA grant 80NSSC18K0772, DOE grant DE-SC0019329, and NNSA grants DE-NA0003914 and DE-NA0003856. J.S. was also supported by DOE grant DE-SC0019329 and NNSA grant DE-NA0003914. E.B. was also supported by DOE grants DE-SC0001063, DE-SC0020432, and DE-SC0020103, and NSF grant AST-1813298. Computing

time was provided by the National Energy Research Scientific Computing Center (NERSC) under contract No. DE-AC02-05CH11231 and by an award from the INCITE program, using resources of the Argonne Leadership Computing Facility, which is a DOE Office of Science User Facility supported under contract DE-AC02-06CH11357.

Appendix A Numerical Setup

Our numerical simulations of mechanically forced turbulence are conducted in a periodic box $\mathbb{T}^3 = [0, L]^3$, with $L = 2\pi$. We use a pseudo-spectral code with phase-shift dealiasing. The time integration method is a second-order Adam–Bashforth scheme. We solve the incompressible MHD equations with hyperviscosity (Borue & Orszag 1995) and hyperresistivity with a Laplacian of exponent $\alpha = 5$:

$$\partial_t \mathbf{u} + (\mathbf{u} \cdot \nabla) \mathbf{u} = -\nabla p + \mathbf{J} \times \mathbf{B} - \nu_h (-\nabla^2)^\alpha \mathbf{u} + \mathbf{f}, \quad (\text{A1})$$

$$\partial_t \mathbf{B} = \nabla \times (\mathbf{u} \times \mathbf{B}) - \eta_h (-\nabla^2)^\alpha \mathbf{B}, \quad (\text{A2})$$

$$\nabla \cdot \mathbf{u} = \nabla \cdot \mathbf{B} = 0, \quad (\text{A3})$$

where ν_h is the hyperviscosity and η_h is the hyperresistivity coefficients. Hyperdiffusivity is commonly used in MHD turbulence studies (Cho & Vishniac 2000; Kawai 2013; Beresnyak 2015; Meyrand et al. 2016; Kawazura et al. 2019) to reduce the dissipation range extent, thereby allowing for a longer inertial-inductive range of scales. The velocity and magnetic field are initialized in k space with $E^{u,b} \sim |\mathbf{k}|^2 e^{-|\mathbf{k}|^2/11}$ spectra and random phases.

Runs I, II, and V (see Table 2 for simulation details) are driven by ABC forcing (named after Arnold, Beltrami, and

Childress):

$$\begin{aligned} \mathbf{f} \equiv & [A \sin(k_f z) + C \cos(k_f y)] \mathbf{e}_x + [B \sin(k_f x) \\ & + A \cos(k_f z)] \mathbf{e}_y + [C \sin(k_f y) + B \cos(k_f x)] \mathbf{e}_z, \end{aligned} \quad (\text{A4})$$

where $A = B = C = 0.25$, k_f is the forcing wavenumber, and \mathbf{e}_x , \mathbf{e}_y , and \mathbf{e}_z are unit vectors in x , y , and z , respectively. ABC forcing is helical, which injects kinetic helicity into the flow. Kinetic helicity is an example of a pseudoscalar that facilitates large-scale dynamos (e.g., Parker 1955; Moffatt 1978; Mininni & Montgomery 2005; Blackman 2016).

Taylor–Green (TG) forcing, which is nonhelical, is used to drive the flow in Runs III and IV:

$$\begin{aligned} \mathbf{f} \equiv & f_0 [\sin(k_f x) \cos(k_f y) \cos(k_f z) \mathbf{e}_x \\ & - \cos(k_f x) \sin(k_f y) \cos(k_f z) \mathbf{e}_y], \end{aligned} \quad (\text{A5})$$

where the force amplitude $f_0 = 0.25$. TG forcing injects no global integrated kinetic helicity into the flow.

The simulations are conducted at different Reynolds numbers with different grid resolutions. Detailed parameters are shown in Table 2, where the subscripts a, b, c, and d (e.g., Run V_a versus V_b versus V_c versus V_d) denote simulations using the same parameters but at different grid resolutions and Reynolds numbers. Runs I–IV are conducted with grid resolution of 256^3 , 512^3 , and 1024^3 . Run V is also conducted at 2048^3 resolution. For Run III, $\text{Pr}_m = 0.1$, $\text{Pr}_m = 5$, and $\text{Pr}_m = 10$ at grid resolution of 256^3 and 512^3 are added to study the effects of a non-unity microscopic Prandtl number.

Figure 5 visualizes the magnitude of the velocity and magnetic fields ($|\mathbf{u}|$ and $|\mathbf{B}|$) in two simulations. The anisotropic structures are significant in the presence of an external magnetic field (Figures 5(c) and (d)).

Figure 6 shows that C_u and C_b used in Equations (21) and (23) are indeed proportionality constants that are scale independent within the decoupled range.

Table 2
Simulations Parameters: Pr_m is the Magnetic Prandtl Number

Run	Grid	Forcing	k_f	Pr_m	$ B_0 /B_k^{\max}$	ν_h	η_h
I_a	256^3	ABC	2	1	0	5×10^{-16}	5×10^{-16}
I_b	512^3	ABC	2	1	0	2×10^{-21}	2×10^{-21}
I_c	1024^3	ABC	2	1	0	4×10^{-25}	4×10^{-25}
II_a	256^3	ABC	2	1	10	5×10^{-16}	5×10^{-16}
II_b	512^3	ABC	2	1	10	2×10^{-21}	2×10^{-21}
II_c	1024^3	ABC	2	1	10	4×10^{-25}	4×10^{-25}
III_a	256^3	TG	1	1	0	5×10^{-16}	5×10^{-16}
III_b	512^3	TG	1	1	0	2×10^{-21}	2×10^{-21}
III_c	1024^3	TG	1	1	0	4×10^{-25}	4×10^{-25}
IV_a	256^3	TG	1	2	0	2×10^{-16}	1×10^{-16}
IV_b	512^3	TG	1	2	0	4×10^{-21}	2×10^{-21}
IV_c	1024^3	TG	1	2	0	4×10^{-25}	2×10^{-25}
$IV_a(\text{Pr}_m = 0.1)$	256^3	TG	1	0.1	0	2×10^{-17}	2×10^{-16}
$IV_b(\text{Pr}_m = 0.1)$	512^3	TG	1	0.1	0	2×10^{-21}	2×10^{-20}
$IV_a(\text{Pr}_m = 5)$	256^3	TG	1	5	0	1×10^{-16}	2×10^{-17}
$IV_b(\text{Pr}_m = 5)$	512^3	TG	1	5	0	1×10^{-20}	2×10^{-21}
$IV_a(\text{Pr}_m = 10)$	256^3	TG	1	10	0	2×10^{-16}	2×10^{-17}
$IV_b(\text{Pr}_m = 10)$	512^3	TG	1	10	0	2×10^{-20}	2×10^{-21}
V_a	256^3	ABC	2	1	2	5×10^{-16}	5×10^{-16}
V_b	512^3	ABC	2	1	2	2×10^{-21}	2×10^{-21}
V_c	1024^3	ABC	2	1	2	4×10^{-25}	4×10^{-25}
V_d	2048^3	ABC	2	1	2	1×10^{-27}	1×10^{-27}

Note. $B_k^{\max} = \sqrt{\max_k [E^b(k)]}$ is at the magnetic spectrum's $[E^b(k)]$ peak. ABC (helical) and TG (nonhelical) forcing are applied at wavenumber k_f .

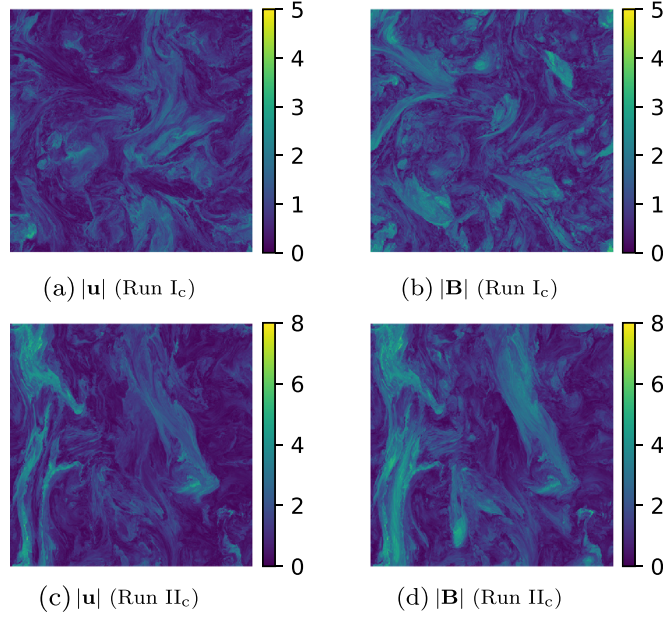


Figure 5. Slices of the magnitude of velocity field $|\mathbf{u}|$ and magnetic field $|\mathbf{B}|$. Panels (a) and (b) show results from Run I_c without an external B field $|B_0| = 0$. Panels (c) and (d) show results from Run II_c with $|B_0| = 10$. The plots show significant anisotropic structures in Run II_c.

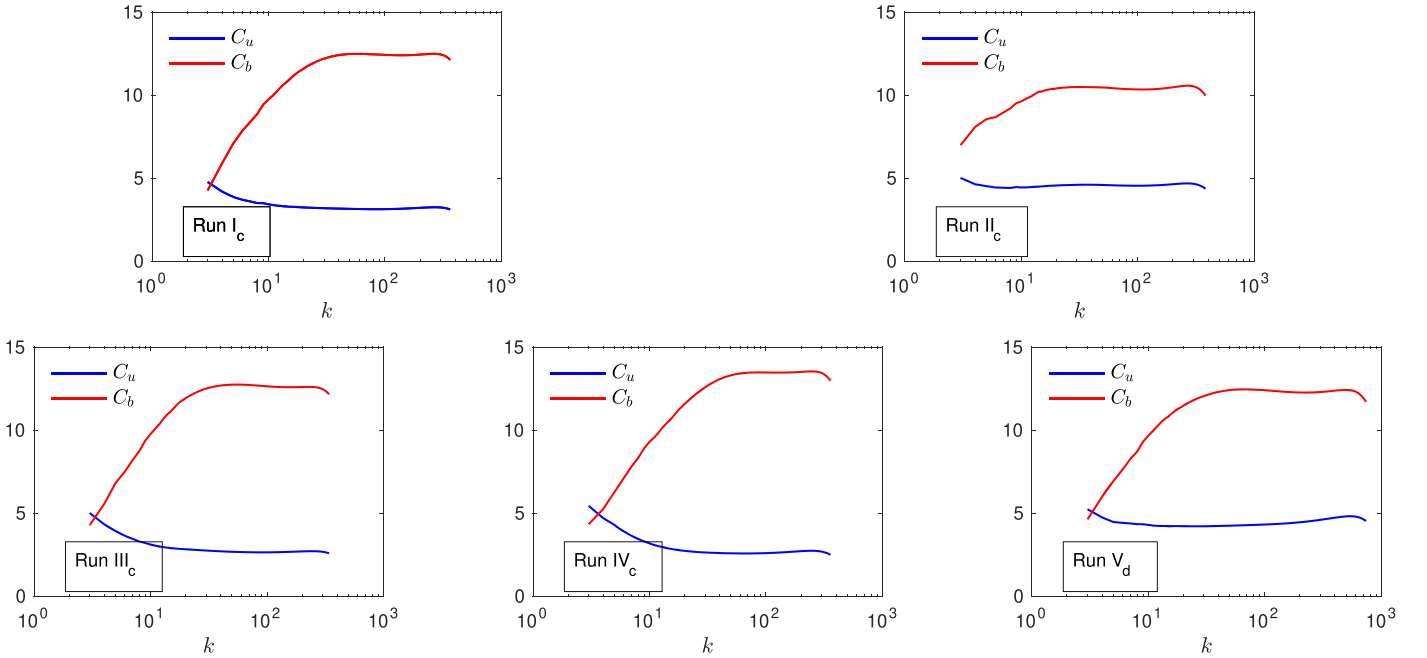


Figure 6. Plots showing C_u and C_b of Runs I–V at the highest resolution. C_b is calculated with $\sigma_b = 1/3$. C_u is calculated with $\sigma_u = 1/4$ in Run II_c and Run V_d and $\sigma_u = 1/6$ in other cases.

Appendix B Helical Forcing Results

The section shows numerical results from simulations with helical forcing. The α -effect of dynamo theory is believed to be important in helical turbulence. We show here the helically forced results for completeness, although ignoring the α term in Equation (7) may not be justified. Nevertheless, our results are remarkably similar to those in the main text.

Figure 7 shows ν_t , η_t , and Pr_t scaling at the highest resolution in helical forcing simulations, as a supplement to Figures 1(a) and (b). The results are $\nu_t(k) \sim k^{-5/3}$ (or $\sim k^{-3/2}$) and $\eta_t(k) \sim k^{-4/3}$,

and $\text{Pr}_t(k) \sim k^{-1/3}$ (or $\sim k^{-1/6}$), similar to the nonhelical simulation results. As we mention in the main section, σ_u is $\approx 1/4$ rather than $1/6$ in the presence of a strong external B field (Run II), leading to the change in the scaling of ν_t and Pr_t .

Figure 8 shows $\langle \overline{\Pi}_\ell^u \rangle / \langle \overline{\Pi}_\ell^b \rangle$ and $\langle |\overline{\mathcal{J}}_\ell|^2 \rangle / \langle 2|\overline{\mathcal{S}}_\ell|^2 \rangle$ at the highest resolution in helical forcing simulations, as a supplement to Figure 2. The results suggest constant $\langle \overline{\Pi}_\ell^u \rangle / \langle \overline{\Pi}_\ell^b \rangle$ in the decoupled range and the same scaling of $\langle |\overline{\mathcal{J}}_\ell|^2 \rangle / \langle 2|\overline{\mathcal{S}}_\ell|^2 \rangle$ and Pr_t in the decoupled range, similar to the nonhelical simulation results. The scaling of $\langle |\overline{\mathcal{J}}_\ell|^2 \rangle / \langle 2|\overline{\mathcal{S}}_\ell|^2 \rangle$ is explained in the main section.

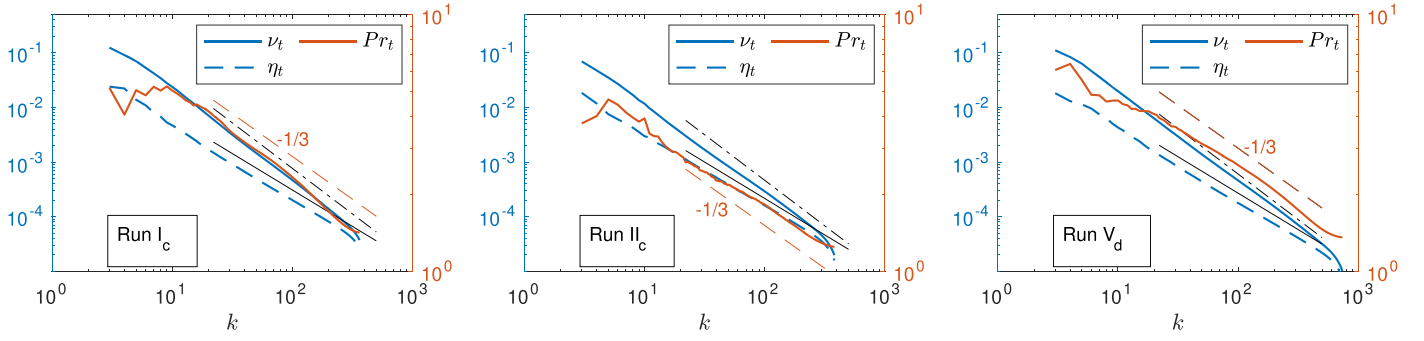


Figure 7. Plots showing turbulent viscosity ν_t , turbulent resistivity η_t , and turbulent magnetic Prandtl number Pr_t calculated using their respective definitions in Equations (6)–(8), at different scales $k = L/\ell$. We use the highest-resolution runs of Runs I, II, and V (ABC forcing) in Table 1. Three reference lines with a slope of $-1/3$, $-5/3$ (black dashed-dotted), and $-4/3$ (black solid) are added. Note the reference line of $-1/3$ and Pr_t uses the right y-axis, while others use the left y-axis. Scales $< \ell_d$ are not shown.

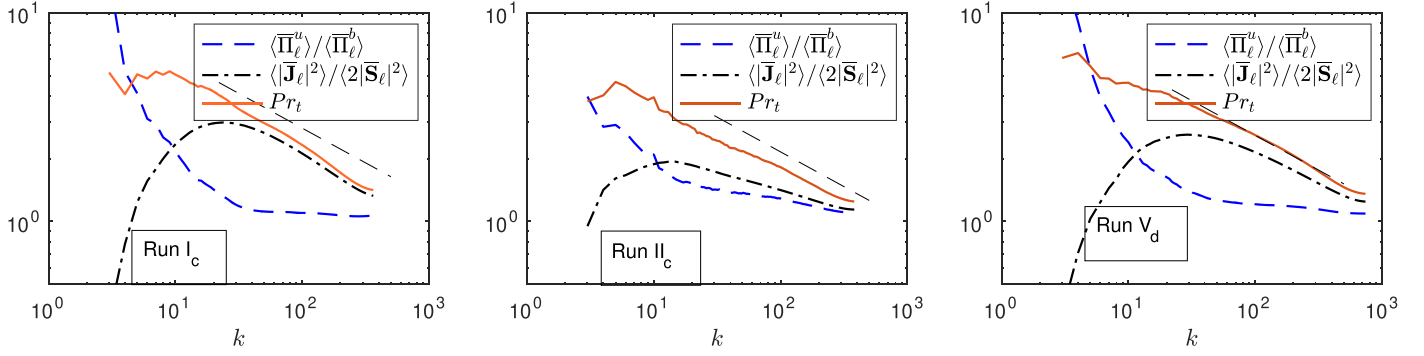


Figure 8. Plots showing the turbulent magnetic Prandtl number Pr_t and its two components $\langle \Pi_\ell^u \rangle / \langle \Pi_\ell^b \rangle$ and $\langle |\mathbf{J}_\ell|^2 \rangle / \langle 2|\mathbf{S}_\ell|^2 \rangle$ at the highest resolutions of Run I, II, and V (ABC forcing) in Table 1. A reference line with a slope of $-1/3$ (black dashed) is added. The plots show that $\langle \Pi_\ell^u \rangle / \langle \Pi_\ell^b \rangle$ approaches a constant in the decoupled range. Note that with a strong external B field (Run II), we expect $\langle \Pi_\ell^u \rangle / \langle \Pi_\ell^b \rangle$ to plateau at sufficiently high Reynolds numbers (Bian & Aluie 2019).

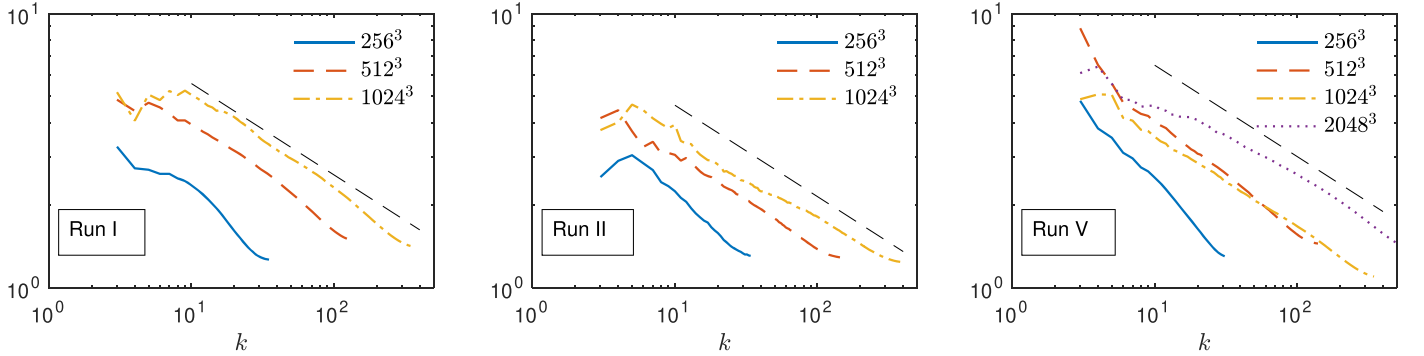


Figure 9. Plots showing the turbulent magnetic Prandtl number Pr_t at different Reynolds numbers (grid resolution) of Runs I, II, and V (ABC forcing) in Table 1. A reference line with a slope of $-1/3$ (black dashed) is added.

Figure 9 shows Pr_t at different Reynolds number in helical forcing simulations, as a supplement to Figure 4. The results are similar to nonhelical simulation results.

Appendix C Results at Different Reynolds Numbers

Figure 10 shows the kinetic energy spectrum at different Reynolds numbers (grid resolution). The slope becomes steeper as the Reynolds number increases. The slope is near $-3/2$ at the highest resolution in Run II and Run V (with external B field), while shallower than $-3/2$ in other simulations. Grete et al. (2021)

observed a kinetic energy spectrum of $-4/3$, which is also shallower than $-3/2$.

Figure 11 shows the magnetic energy spectrum at different Reynolds numbers. The slope agrees well with $-5/3$ for all Reynolds numbers. Figure 12 shows the kinetic and magnetic energy spectra of Run IV with $Pr_m = 0.1, 5, \text{ and } 10$.

Figure 13 shows that the scaling exponent of ν_t is near $-5/3$ ($-3/2$ in Run II_c and V_d) at the highest resolution. As the Reynolds number increases, it becomes steeper and approaches $-3/2$. Figure 14 shows the scaling exponent of η_t at all Reynolds numbers is near $-4/3$, consistent with Equation (14).

Figure 15 shows $\langle \Pi_\ell^u \rangle / \langle \Pi_\ell^b \rangle$ and $\langle |\mathbf{J}_\ell|^2 \rangle / \langle 2|\mathbf{S}_\ell|^2 \rangle$ at different Reynolds numbers (grid resolution).

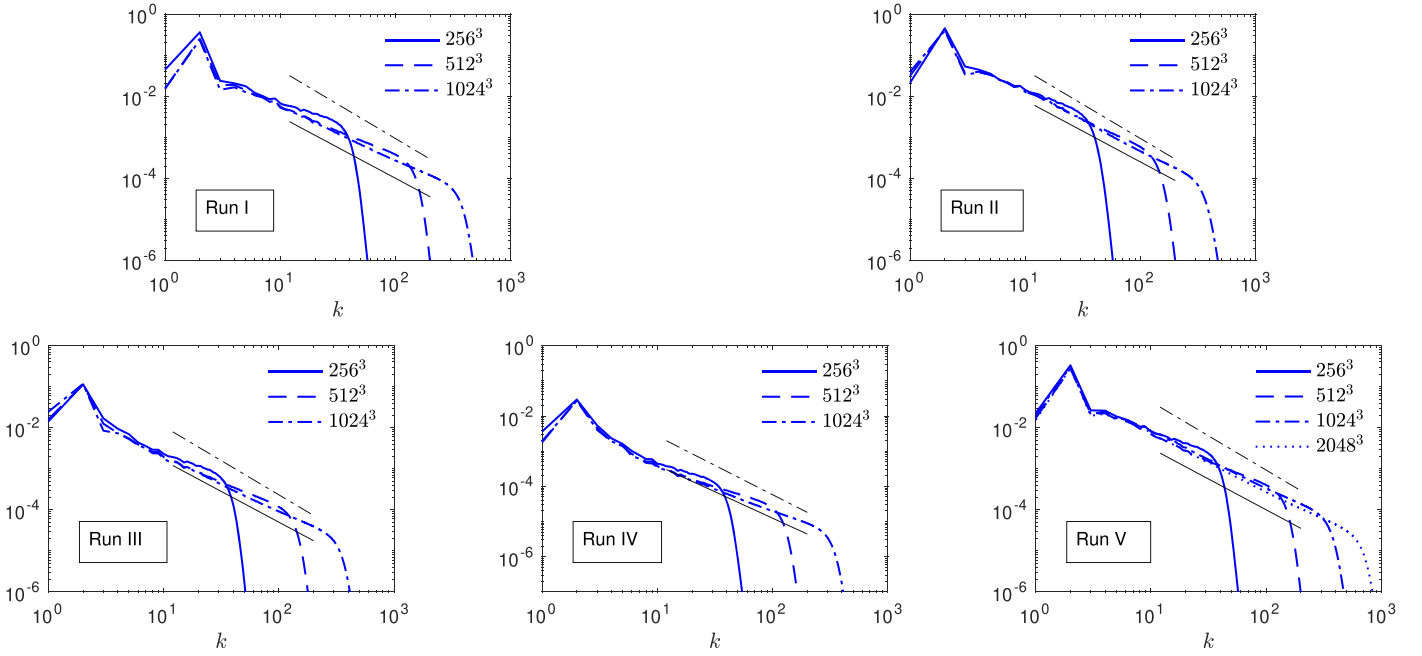


Figure 10. Plots showing the kinetic energy spectrum $E^u(k)$ at different Reynolds numbers (grid resolution) of Runs I–V. We show two reference lines with a slope of $-3/2$ (black solid) and $-5/3$ (black dashed–dotted). The slope becomes steeper as the Reynolds number increases. The slope is near $-3/2$ at the highest resolution in Run II and Run V (with external B field) while shallower than $-3/2$ in other simulations. Note Grete et al. (2021) observed a kinetic energy spectrum of $-4/3$, which is also shallower than $-3/2$.

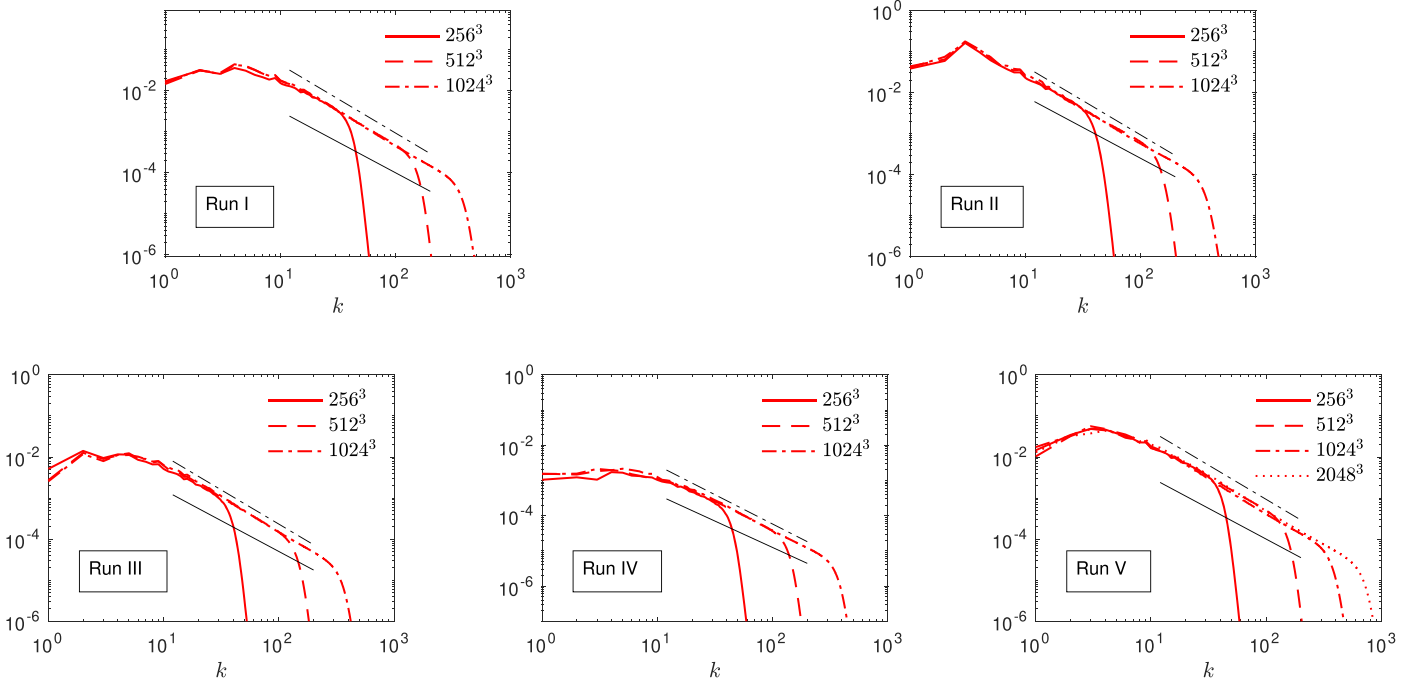


Figure 11. Plots showing the magnetic energy spectrum $E^b(k)$ at different Reynolds numbers (grid resolution) of Runs I–V. We show two reference lines with a slope of $-3/2$ (black solid) and $-5/3$ (black dashed–dotted). The slope of the magnetic spectrum agrees well with solar wind observations ($-5/3$).

Figure 16 shows the Pr_t at different Reynolds numbers with the x -axis normalized by $k_d = L/\ell_d$, where ℓ_d is defined as the scale at which $\langle \bar{\Pi}_\ell^u + \bar{\Pi}_\ell^b \rangle = \nu \langle |\nabla \bar{u}|^2 \rangle + \eta \langle |\nabla \bar{B}|^2 \rangle$. For non-unity Pr_m , $\ell_d \equiv \max(\ell_\nu, \ell_\eta)$. ℓ_ν and ℓ_η are defined as scales where $\langle \bar{\Pi}_\ell^u \rangle = \nu \langle |\nabla \bar{u}|^2 \rangle$ and $\langle \bar{\Pi}_\ell^b \rangle = \eta \langle |\nabla \bar{B}|^2 \rangle$. Pr_t at different Reynolds numbers collapse at $k = k_d$, as expected (see also Table 3).

Figure 17 shows $\langle \bar{\Pi}_\ell^u \rangle / \langle \bar{\Pi}_\ell^b \rangle$ at different microscopic Prandtl numbers ($\text{Pr}_m = 0.1, 1, 5, 10$). Because the decoupled range, over which each of $\langle \bar{\Pi}_\ell^u \rangle$ and $\langle \bar{\Pi}_\ell^b \rangle$ becomes scale independent, is barely resolved, these plots neither reinforce nor conflict with the expectation of asymptotic equipartition of the kinetic and magnetic cascades predicted in Bian & Aluie (2019), irrespective of microscopic Pr_m . It is worth emphasizing that

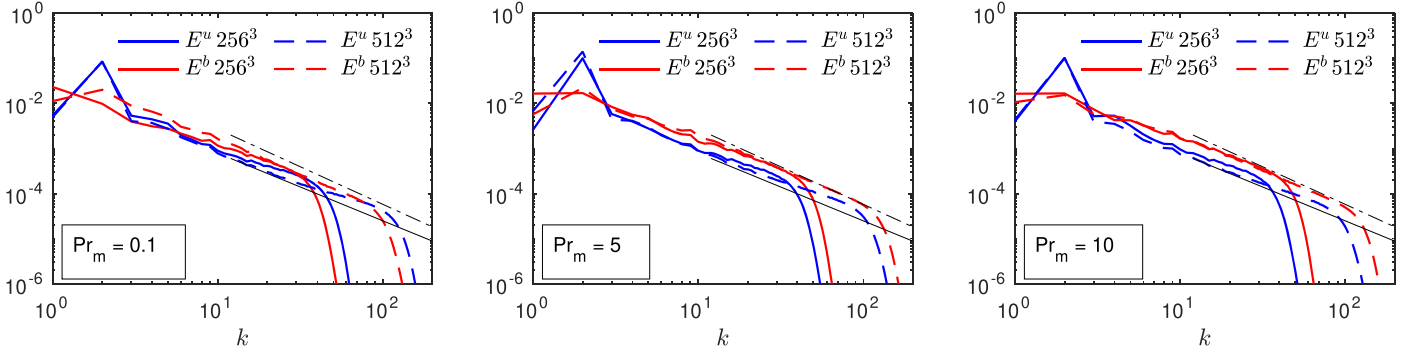


Figure 12. Plots showing kinetic and magnetic energy spectra, $E^u(k)$ and $E^b(k)$, of Run IV with $\text{Pr}_m = 0.1, 5,$ and 10 . We show two reference lines with a slope of $-3/2$ (black solid) and $-5/3$ (black dashed-dotted).

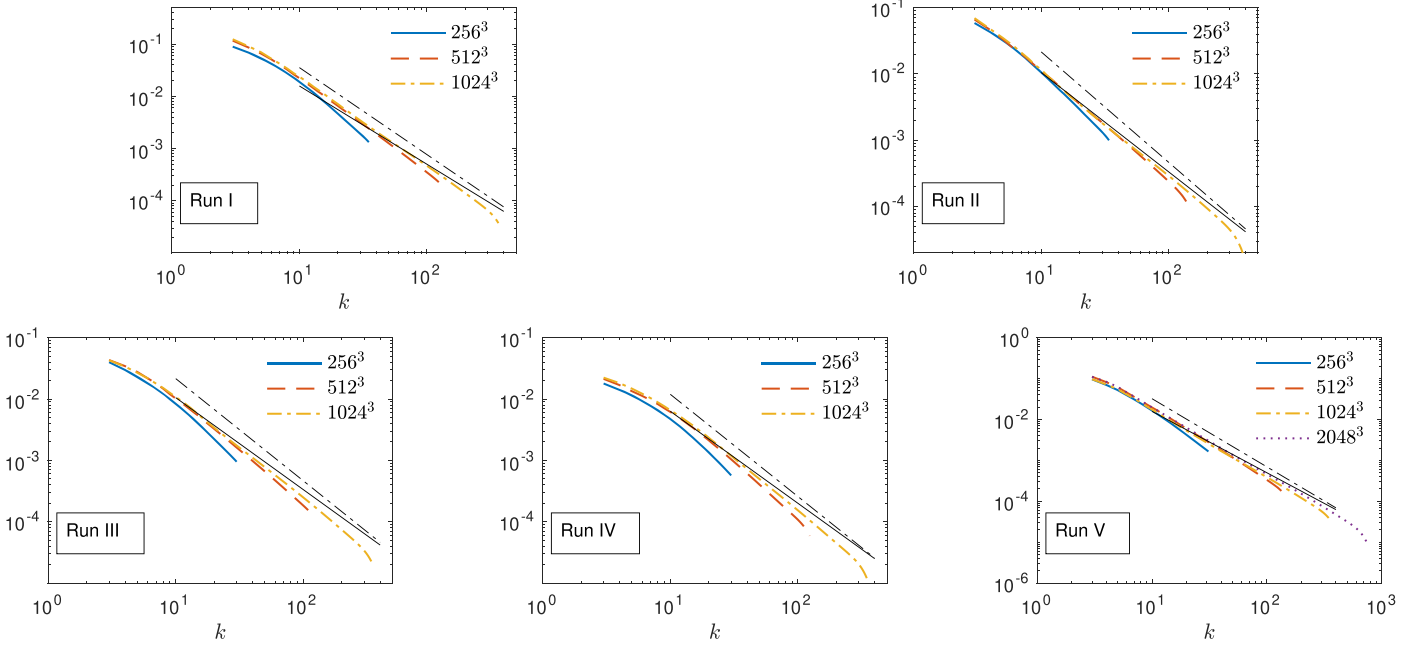


Figure 13. Plots showing the turbulent viscosity ν_t at different Reynolds numbers (grid resolution) of Runs I–V. Reference lines with a slope of $-5/3$ (black dashed-dotted) and $-3/2$ (black solid) are added.

the observation of Brandenburg (2014) of a positive correlation between Pr_m and the ratio of kinetic dissipation to magnetic dissipation does not have a direct bearing on the ratio of the cascades. This is because the cascades $\langle \overline{\Pi}_\ell^u \rangle$ and $\langle \overline{\Pi}_\ell^b \rangle$ in the decoupled range are not necessarily equal to the kinetic and

magnetic energy dissipation, respectively. This is especially true at non-unity Pr_m at scales smaller than ℓ_d beyond the decoupled range, where kinetic-magnetic conversion is expected to occur (e.g., in the viscous-inductive range at high Pr_m) before all energy is dissipated microscopically.

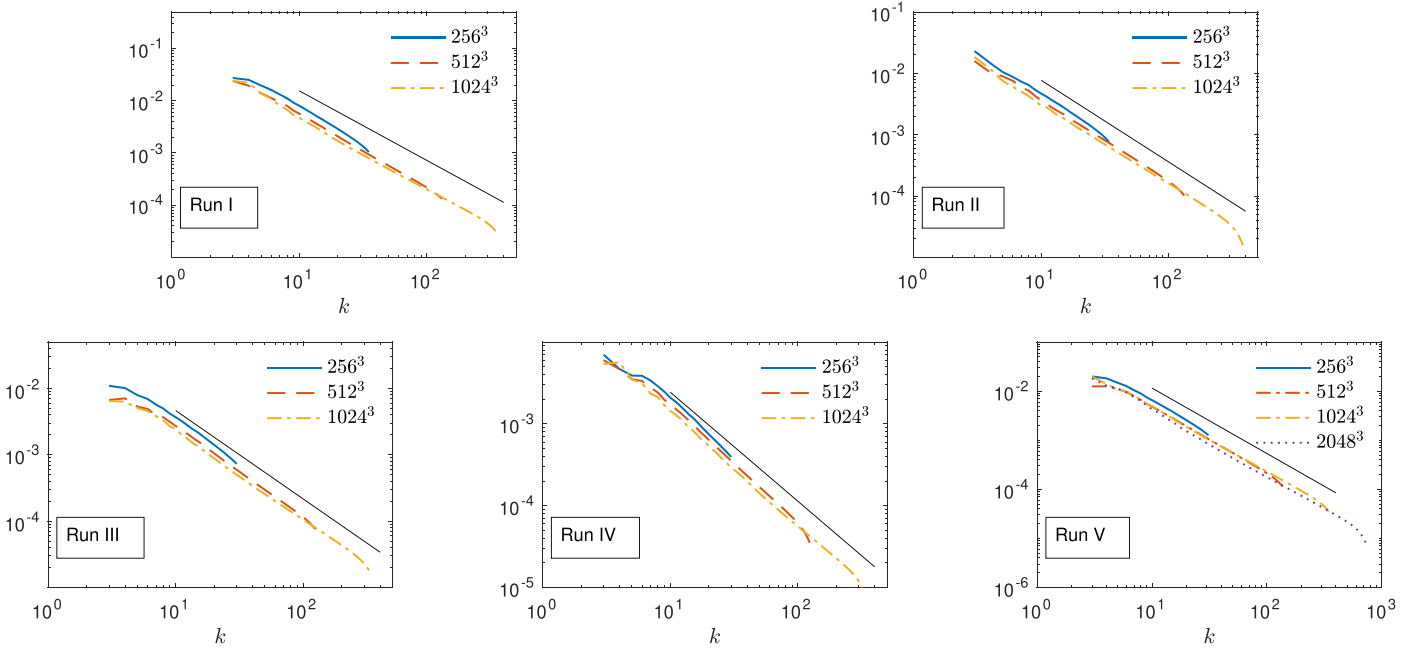


Figure 14. Plots showing the turbulent resistivity η , at different Reynolds numbers (grid resolution) of Runs I–V. A reference line with a slope of $-4/3$ (black solid) is added. The scaling exponent agrees well with the expected value $-4/3$.

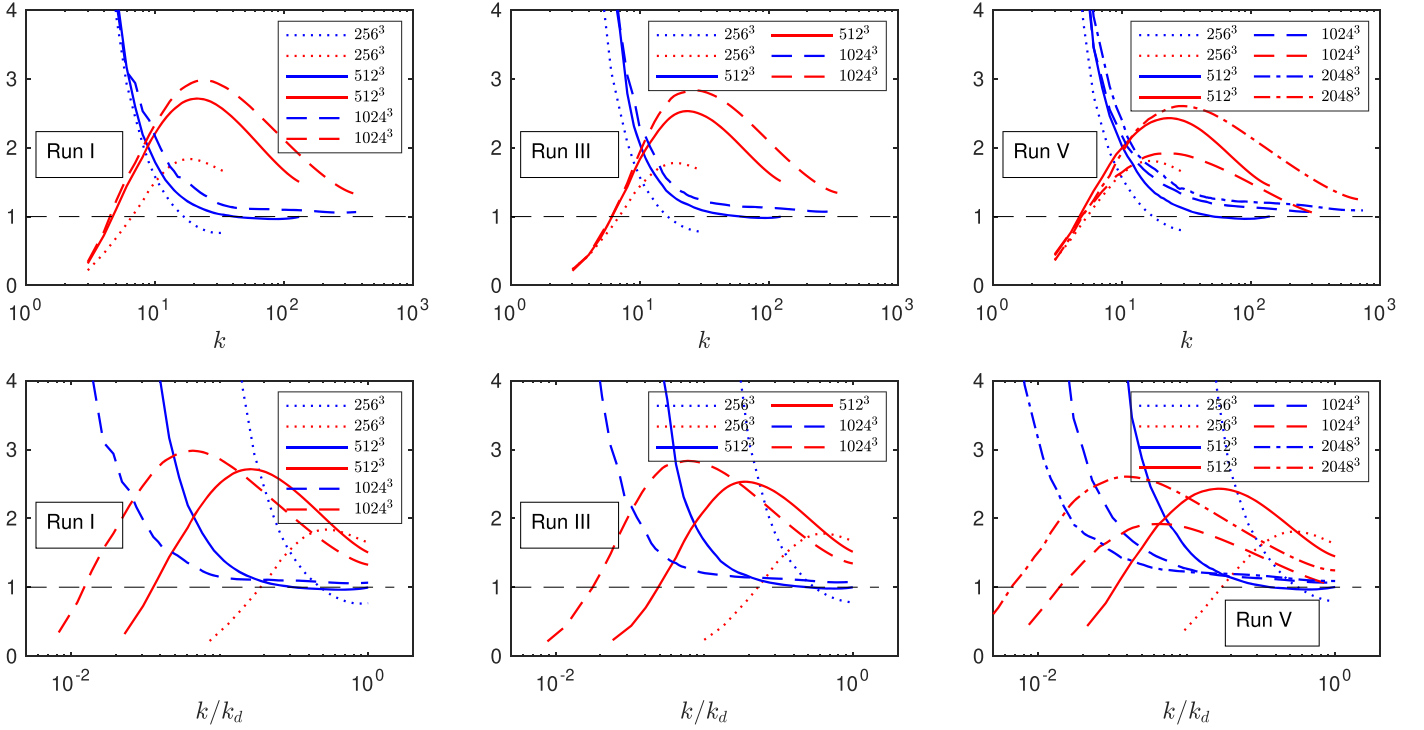


Figure 15. Plots showing $\langle \Pi_t^u \rangle / \langle \Pi_t^b \rangle$ (blue lines) and $\langle |J_i|^2 \rangle / \langle 2|S_i|^2 \rangle$ (red lines) at different Reynolds numbers (grid resolution) of Runs I, III, and V. The x-axis in the bottom panels is normalized by $k_d = L/\ell_d$. A reference line (black dashed) of 1 is added.

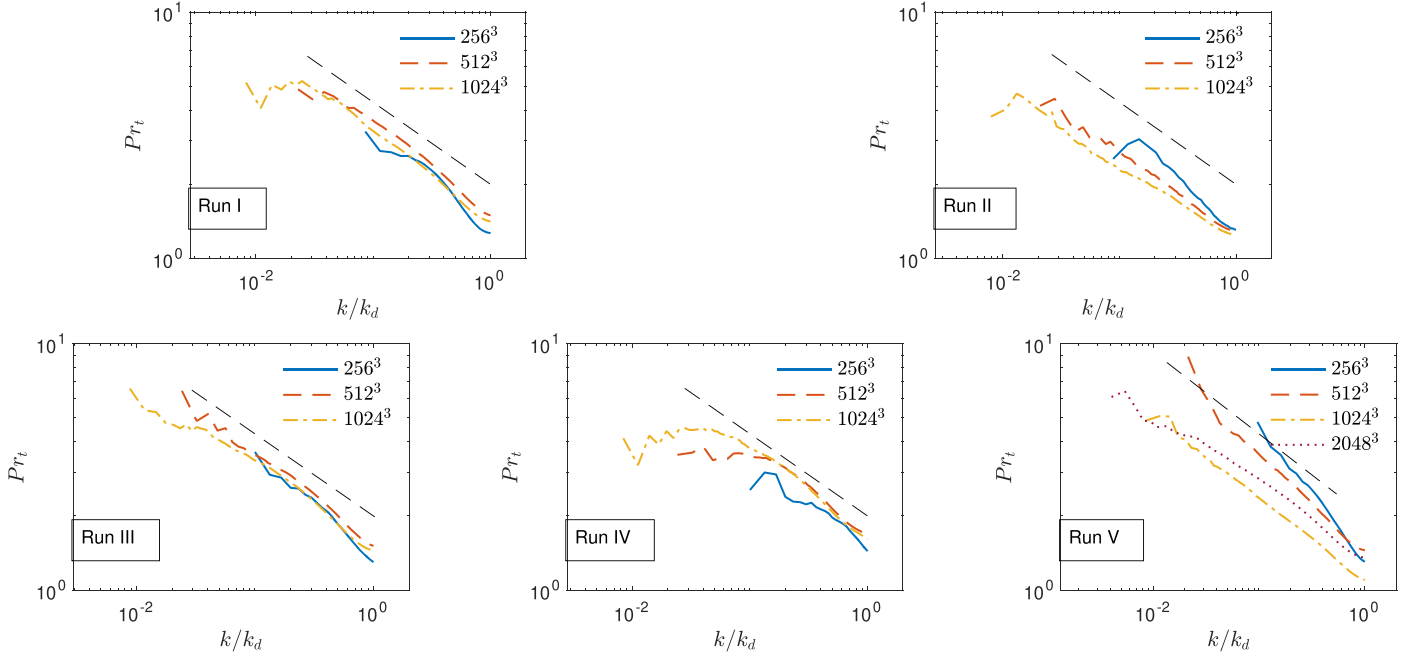


Figure 16. Plots showing the Pr_t at different Reynolds numbers (grid resolution) of Runs I–V with x -axis normalized by $k_d = 2\pi/\ell_d$. A reference line with a slope of $-1/3$ (black dashed) is added. Pr_t at different Reynolds numbers collapse at $k = k_d$, as expected (see also Table 3).

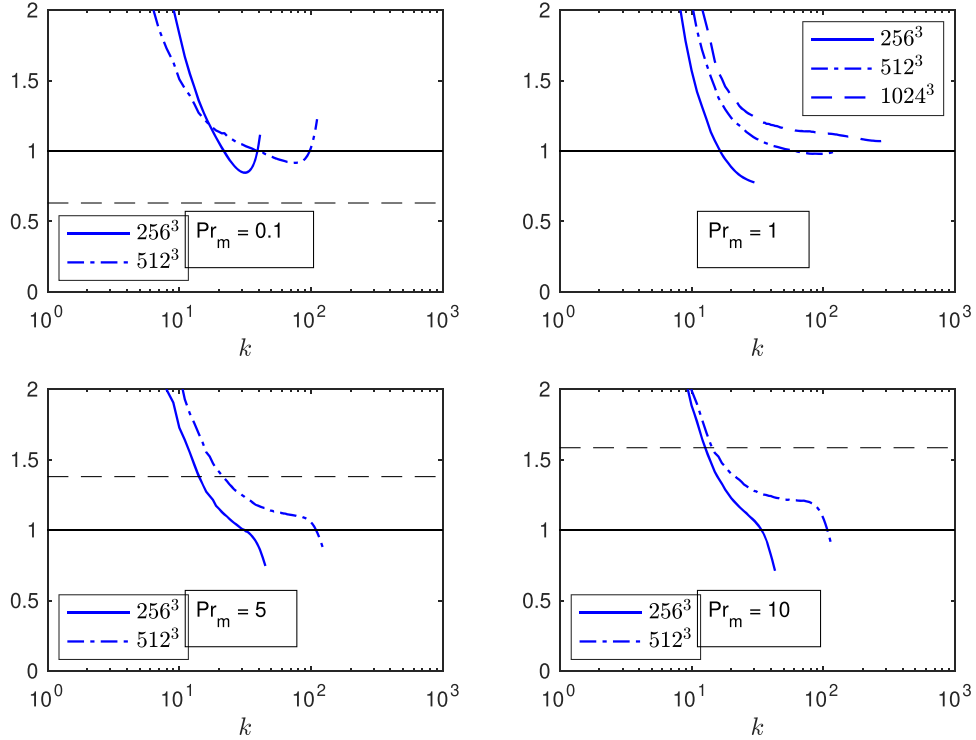


Figure 17. Plots showing $\langle \overline{\Pi}_\ell^u \rangle / \langle \overline{\Pi}_\ell^b \rangle$ at different microscopic Prandtl numbers ($Pr_m = 0.1, 1, 5, 10$). The parameters are detailed in Table 2. These simulations are conducted on a 512^3 grid. A reference line (black solid) of 1 is added in all panels. Note our usage of fifth-order hyperdiffusion in the simulations. Another reference line (black dashed) of $\nu_h^{1/5}/\eta_h^{1/5}$ is added as an estimate for the microscopic magnetic Prandtl number corresponding to normal (Laplacian) diffusion. The estimate is 0.63, 1, 1.38, and 1.58 for $Pr_m = 0.1$, $Pr_m = 1$, $Pr_m = 5$, and $Pr_m = 10$, respectively. Because the decoupled range, over which $\langle \overline{\Pi}_\ell^u \rangle$ and $\langle \overline{\Pi}_\ell^b \rangle$ become scale independent, is barely resolved, these plots neither reinforce nor conflict with the expectation of asymptotic equipartition of the kinetic and magnetic cascades predicted in Bian & Aluie (2019), irrespective of microscopic Pr_m .

Table 3
 Pr_t at $k/k_d = 1$, where $k_d = L/\ell_d$

	Run I	Run II	Run III	Run IV	Run V
256^3	1.23	1.31	1.40	1.44	1.30
512^3	1.50	1.29	1.45	1.68	1.45
1024^3	1.41	1.25	1.51	1.67	1.10
2048^3					1.36

ORCID iDs

Xin Bian  <https://orcid.org/0000-0002-7020-475X>
 Jessica K. Shang  <https://orcid.org/0000-0003-1466-7108>
 Eric G. Blackman  <https://orcid.org/0000-0002-9405-8435>
 Gilbert W. Collins  <https://orcid.org/0000-0002-4883-1087>
 Hussein Aluie  <https://orcid.org/0000-0003-3516-3697>

References

- Aluie, H. 2017, *NJPh*, **19**, 025008
 Aluie, H., & Eyink, G. L. 2010, *PhRvL*, **104**, 081101
 Balbus, S. A., & Hawley, J. F. 1998, *RvMP*, **70**, 1
 Beresnyak, A. 2015, *ApJL*, **801**, L9
 Bian, X., & Aluie, H. 2019, *PhRvL*, **122**, 135101
 Biskamp, D. 2003, *Magnetohydrodynamic Turbulence* (Cambridge: Cambridge Univ. Press)
 Blackman, E. G. 2016, *Magnetic Helicity and Large Scale Magnetic Fields: A Primer* (Berlin: Springer)
 Blackman, E. G., & Nauman, F. 2015, *JPIPh*, **81**, 395810505
 Blandford, R. D., & Payne, D. G. 1982, *MNRAS*, **199**, 883
 Blandford, R. D., & Znajek, R. L. 1977, *MNRAS*, **179**, 433
 Boldyrev, S. 2005, *ApJL*, **626**, L37
 Boldyrev, S. 2006, *PhRvL*, **96**, 115002
 Boldyrev, S., & Perez, J. C. 2009, *PhRvL*, **103**, 225001
 Boldyrev, S., Perez, J. C., Borovsky, J. E., & Podesta, J. J. 2011, *ApJL*, **741**, L19
 Borovsky, J. E. 2012, *JGRA*, **117**, A05104
 Borue, V., & Orszag, S. A. 1995, *EL*, **29**, 687
 Boussinesq, J. 1877, *Essai sur la théorie des eaux courantes* (Paris: Impr. Nationale)
 Brandenburg, A. 2014, *ApJ*, **791**, 12
 Brandenburg, A., & Rempel, M. 2019, *ApJ*, **879**, 57
 Cao, X. 2011, *ApJL*, **737**, 94
 Chernyshov, A., Karelsky, K., & Petrosyan, A. 2007, *PhFl*, **19**, 055106
 Cho, J., & Vishniac, E. T. 2000, *ApJ*, **539**, 273
 Davidson, P. A., Kaneda, Y., & Sreenivasan, K. R. 2012, *Ten Chapters in Turbulence* (Cambridge: Cambridge Univ. Press) doi:10.1017/CBO9781139032810
 Elmegreen, B. G., & Scalo, J. 2004, *ARA&A*, **42**, 211
 Eyink, G., Vishniac, E., Lalescu, C., et al. 2013, *Natur*, **497**, 466
 Eyink, G. L. 2005, *PhyD*, **207**, 91
 Eyink, G. L. 2018, arXiv:1803.02223
 Forster, D., Nelson, D. R., & Stephen, M. J. 1977, *PhRvA*, **16**, 732
 Fournier, J.-D., Sulem, P.-L., & Pouquet, A. 1982, *JPhA*, **15**, 1393
 Frisch, U., Kurien, S., Pandit, R., et al. 2008, *PhRvL*, **101**, 144501
 Fromang, S., & Stone, J. M. 2009, *A&A*, **507**, 19
 Goldreich, P., & Sridhar, S. 1995, *ApJ*, **438**, 763
 Grappin, R., Müller, W.-C., & Verdini, A. 2016, *A&A*, **589**, A131
 Grete, P., Glines, F. W., & O'Shea, B. W. 2020, *IEEE Transactions on Parallel and Distributed Systems*, **32**, 85
 Grete, P., O'Shea, B. W., & Beckwith, K. 2021, *ApJ*, **909**, 148
 Grete, P., Vlaykov, D. G., Schmidt, W., Schleicher, D. R., & Federrath, C. 2015, *NJPh*, **17**, 023070
 Guan, X., & Gammie, C. F. 2009, *ApJ*, **697**, 1901
 Haugen, N. E. L., Brandenburg, A., & Dobler, W. 2004, *PhRvE*, **70**, 016308
 Iroshnikov, P. 1963, *AZh*, **40**, 742
 Jafari, A., & Vishniac, E. T. 2018, *ApJ*, **854**, 2
 Käpylä, M. J., Rheinhardt, M., & Brandenburg, A. 2021, arXiv:2106.01107
 Käpylä, P., Korpi, M., & Bran666denburg, A. 2009, *A&A*, **500**, 633
 Käpylä, P., Rheinhardt, M., Brandenburg, A., & Käpylä, M. J. 2020, *A&A*, **636**, A93
 Kawai, S. 2013, *JCoPh*, **251**, 292
 Kawazura, Y., Barnes, M., & Schekochihin, A. A. 2019, *PNAS*, **116**, 771
 Kitchatinov, L., Pipin, V., & Rüdiger, G. 1994, *AN*, **315**, 157
 Kolmogorov, A. N. 1941, *DoSSR*, **30**, 301
 Kraichnan, R. H. 1965, *PhFl*, **8**, 1385
 Kuhlén, M., Woosley, S., & Glatzmaier, G. 2006, *ApJ*, **640**, 407
 Lesur, G., & Longaretti, P.-Y. 2007, *MNRAS*, **378**, 1471
 Lesur, G., & Longaretti, P. Y. 2009, *A&A*, **504**, 309
 Lovelace, R. V. E., Rothstein, D. M., & Bisnovatyi-Kogan, G. S. 2009, *ApJ*, **701**, 885
 Lubow, S. H., Papaloizou, J. C. B., & Pringle, J. E. 1994, *MNRAS*, **267**, 235
 Meneveau, C., & Katz, J. 2000, *AnRFM*, **32**, 1
 Meyrand, R., Galtier, S., & Kiyani, K. H. 2016, *PhRvL*, **116**, 105002
 Miesch, M., Matthaues, W., Brandenburg, A., et al. 2015, *SSRv*, **194**, 97
 Mininni, P. D., & Montgomery, D. C. 2005, *PhRvE*, **72**, 056320
 Mininni, P. D., & Pouquet, A. 2009, *PhRvE*, **80**, 025401
 Moffatt, H. K. 1978, *Magnetic Field Generation in Electrically Conducting Fluids* (Cambridge: Cambridge Univ. Press)
 Müller, W.-C., & Carati, D. 2002, *PhPl*, **9**, 824
 Parker, E. N. 1955, *ApJ*, **122**, 293
 Podesta, J., Roberts, D., & Goldstein, M. 2007, *ApJ*, **664**, 543
 Politano, H., & Pouquet, A. 1998a, *PhRvE*, **57**, R21
 Politano, H., & Pouquet, A. 1998b, *GeoRL*, **25**, 273
 Pope, S. B. 2001, *Turbulent Flows* (Bristol: IOP Publishing)
 Sadek, M., & Aluie, H. 2018, *PhRvF*, **3**, 124610
 Schekochihin, A. A. 2020, arXiv:2010.00699
 Schrunner, M., Rädler, K.-H., Schmitt, D., Rheinhardt, M., & Christensen, U. 2005, *AN*, **326**, 245
 Schrunner, M., Rädler, K.-H., Schmitt, D., Rheinhardt, M., & Christensen, U. R. 2007, *GApFD*, **101**, 81
 Shakura, N. I., & Sunyaev, R. A. 1973, *A&A*, **24**, 337
 Smagorinsky, J. 1963, *MWRv*, **91**, 99
 Snellman, J. E., Käpylä, P., Korpi, M., & Liljeström, A. 2009, *A&A*, **505**, 955
 Stone, J. M., Tomida, K., White, C. J., & Felker, K. G. 2020, *ApJS*, **249**, 4
 Tennekes, H., & Lumley, J. 1972, *A First Course in Turbulence* (Cambridge, MA: MIT Press)
 Verma, M. K. 1996, *JGRA*, **101**, 27543
 Verma, M. K. 2001a, *PhPl*, **8**, 3945
 Verma, M. K. 2001b, *PhRvE*, **64**, 026305
 Verma, M. K. 2004, *PhR*, **401**, 229
 Verma, M. K. 2019, *Energy Transfers in Fluid Flows: Multiscale and Spectral Perspectives* (Cambridge: Cambridge Univ. Press)
 Verma, M. K., & Kumar, S. 2004, *Prama*, **63**, 553
 Yousef, T., Brandenburg, A., & Rüdiger, G. 2003, *A&A*, **411**, 321
 Zhao, D., & Aluie, H. 2018, *PhRvF*, **3**, 054603
 Zhou, Y. 2010, *PhR*, **488**, 1
 Zhou, Y., Matthaues, W., & Dmitruk, P. 2004, *RvMP*, **76**, 1015
 Zhou, Y., Schilling, O., & Ghosh, S. 2002, *PhRvE*, **66**, 026309
 Zhu, Z., & Stone, J. M. 2018, *ApJ*, **857**, 34